UNIVERSITÀ DEGLI STUDI DI PADOVA

Dipartimento di Fisica e Astronomia "Galileo Galilei"

Corso di Laurea Magistrale in Fisica

Tesi di Laurea

A novel Tissue Equivalent Proportional Counter for microdosimetry at nanometer scale

Relatore

Dr. Daniele Mengoni

Correlatore

Dr.sa Valeria Conte

Laureando

Lorenzo Longo

Anno Accademico 2017/2018

Contents

Chapter 1

Introduction

Microdosimetry and track-nanodosimetry belong to a recent branch of nuclear physics which developed in the fifties with the first papers by Rossi and others. This new field concerns the study of theoretical and experimental methodologies able to perform a detailed analysis of the radiation interaction with matter, in particular with biological tissue at cellular and sub-cellular level.

The analysis and data brought by this kind of study have a direct impact in various applications, such as radiology, radiotherapy, radiation protection and radiobiology. In radiotherapy the treatment planning aims to deliver sufficient radiation to the tumour while sparing critical organs and minimizing the doze to healthy tissue. The effects of radiation exposure are proportional to the absorbed dose, but they also depend on the type of radiation and the type of biological target. The effects of densely ionizing radiations, which produce a spot pattern of interactions with strong localization of damage, are different from those of sparsely ionizing radiations which produce a uniform pattern of interactions.
Being a macroscopic average quantity, the absorbed dose can not describe the stochastics of energy deposition processes though.
A more detailed knowledge of the local interaction can be achieved by exploiting the methodologies and instruments provided by microdosimetry and nanodosimetry, the former aiming at characterizing the statistical fluctuations of the local energy imparted at the micrometric level, the latter devoted to the description of the pattern of particle interactions at the nanometric level.

To date, the Tissue Equivalent Proportional Counter (TEPC) is the most accurate device able to measure the microdosimetric properties of ionizing processes, and it has showed to properly mimic the corresponding relative biological effectiveness (RBE). The procedure requires application of an empirical weighting function which must be characterized for any specific radiation type and biological target.

The biological damage induced by radiation starts with injuries to sub-cellular structures, such as the chromatin fibers and the DNA segments, therefore the cell damage is strictly related to the spatial distribution of the interaction points between the charged particle and matter. Since this track structure plays a significant role at the nanometer level, the microdosimetric approach, which is based on the local energy imparted to sensitive volumes of matter at micrometer length scale, is not able to provide detailed information about that. Common TEPCs, in fact, are able to measure single event spectra in micrometric sites, down to about 300 nm.

The nanodosimetric quantities demonstrated to have a strong correlation with radiation-induced damages to the DNA. The pattern of particle interactions at the nanometer level is measured by track-nanodosimeters, which derive the single-event distribution of ionization cluster size for sites of a few nanometers up to 20 nm. One of this devices is the so-called StarTrack apparatus, installed at the Tandem-Alpi accelerator complex of LNL, and measuring the number of ionizations produced in nanometric volumes by counting the electrons set free in the ionizing processes. Unfortunately all the present nanodosimeters (only three different prototypes worldwide) are cumbersome (more than $1\,m^3$), and not designed to operate in a clinical environment. From this point of view, a novel TEPC able to simulate down to the nanometer level, could be a portable detector to measure some significant characteristics of the particle track structure. A prototype of a TEPC at the nanometer level has been recently developed and tested on neutron, proton and carbon ion radiation fields down to 25 nm. The response of the TEPC has to be analysed by taking into account the gas avalanche process, which convolutes with the stochastics of the physical interaction within the sensitive volume.

1.1 Goal of the Thesis

In order to characterize the response function of the TEPC in the nanometric domain, simultaneous measurements with the StarTrack track-nanodosimeter should be performed and analysed for different radiation qualities.
This aim requires the design and assembly of another TEPC able to work down to the nanometric scale, which could both fit in the StarTrack apparatus and permit a direct comparison with the microdosimetric spectra produced by its prototype. In particular, the new detector should be characterized by a similar sensitive volume and analogous response to various radiation fields with respect to its precursor. Moreover, it has to be partially wall-less: since the Tandem-Alpi acceleration facility in LNL provides a maximum of 20 MeV/amu accelerated ions, the top and down closure surfaces of the detector have to be drilled in order to allow the particle beam to penetrate through its sensitive volume.
If this new TEPC would demonstrate to properly work in the nanometric domain, a direct comparison between the microdosimeric characteristics measured by this peculiar detector could be transferred to a track-nanodosimetric description, much more relevant in the framework of the biological damages to the nanometric targets.

The aim of this thesis is the construction of this novel TEPC and the execution of the first function test measurements inside the StarTrack apparatus.
Installed on a movable platform, the TEPC can be translated ortogonally to the particle beam in order to scan the sensitive volume of the detector and describe its response as a function of the radial distance from the anode. A beam collimator system and a trigger detector will allow to define the primary particle trajectory. The resolution is that of the beam collimation system, which presently has a diameter of 0.8 mm.

Chapter 2

Microdosimetry and Track-Nanodosimetry

2.1 Radiation Damage and Hadron Therapy

The interaction of ionizing radiation with micro- and nano-metric targets of biological tissue is a transversal field of interest for different branches of science such as radiology, radiotherapy, radiation protection and radiobiology.

The sequence of physical, chemical, biochemical and biological processes evolves over a wide time scale (see Figure 2.1), and starts with the physical interaction of radiation with biological targets, such are the DNA ($\sim 2\,\mathrm{nm}$) or the nucleosome ($\sim 10\,\mathrm{nm}$, see Figure 2.2). The pattern of the interactions is therefore crucial to any detailed understanding of the mechanisms that induce the final biological effect [1].

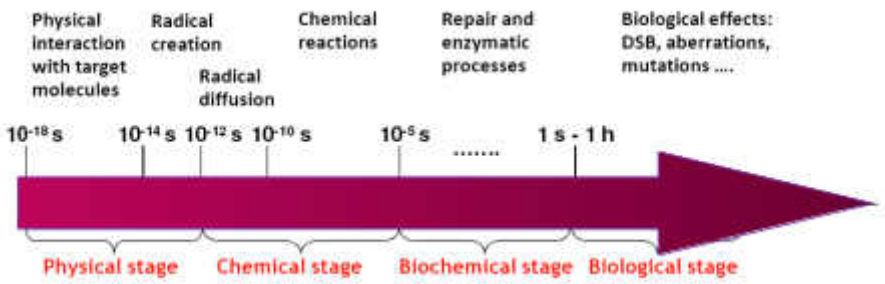

Figure 2.1: Sketch of the typical time scales for the different processes involved in the resulting biological effect. See text for details.

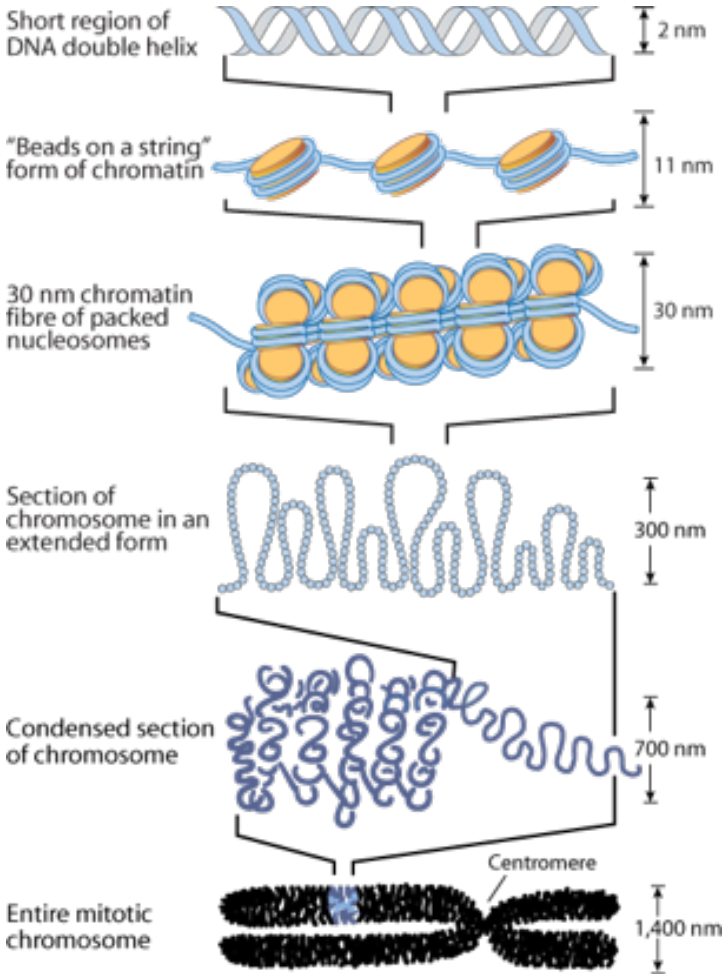

Figure 2.2: Typical dimensions for the biological targets of interest. See text for details.

In the radiotherapy field, a great interest has grown in the last decades for the so-called hadron therapy: a modality based on the exploitation of charged particles (protons and other ions, such as carbon ions) for treating malignant tumours [2], especially for those that show high resistance to conventional treatments like surgery, chemotherapy and traditional radiation therapy with high-energy photons and electrons. The main advantages associated to the use of hadron beams with respect to photon or electron beams are a high ballistic precision, allowing the possibility of treating cancers located near critical organs, the biological effectiveness at a definite absorbed dose and, especially for carbon ions, a lower biological sensitivity to the oxygen content in the tumour.

The standard quantity monitored in the current procedures for clinical dosimetry of proton and ion beams is the absorbed dose to water, which is usually mea-

sured through ionization chambers, calibrated in reference conditions according to dosimetry protocols and experience acquired in conventional radiotherapy [3]. A report produced in 2008 by the International Atomic Energy Agency (IAEA) [4] introduces the difference between the "physical dose distribution" and the "biological dose distribution". The former concept is the measured absorbed dose to water, while the latter is the physical dose distribution weighted by the relative biological effectiveness (RBE) of the beam, which is a correction introduced to take into account the strong dependence of the biological response on the energy of ions. The evaluation of the biological effective dose strongly depends on the RBE value, which in turns is determined by both physical factors and biological processes (such as the particle type and energy, dose, dose per fraction, degree of oxygenations, cell or tissue type and biological end-point considered), and a problem arises in the fact that the numerical RBE evaluation is in principle only valid for the conditions at which it was derived.

The physical component of a particle beam is related to the microscopic track structure, which in its turn depends on the particle type and energy. The biological component depends on the cell response to the distribution of energy deposition and ionization at various geometrical and temporal scales.

From the physical point of view, this means that the measurement of the absorbed dose has to be integrated with information related to the local energy deposition events, which is the trigger for the processes that lead to the biological effect.

A more thorough physical knowledge of the local energy impartation can be accurately performed through the methodologies and instruments provided by:

- microdosimetry, which measures the statistical fluctuations of the local energy imparted at the micrometer level by deriving the single-event distribution of energy transfer [5] [6];
- track-nanodosimetry, which measures the pattern of particle interactions (track structure) at the nanometer level by deriving the single-event distribution of ionization cluster size, defined as the number of ionizations within a site per primary particle [7].

It should be highlighted that, since the birth of track-nanodosimetry, these two fields have proceeded in parallel, without the possibility of a direct comparison between of the results of each other.

2.2 Fundamentals of Microdosimetry

Microdosimetry, which was developed as a system of concepts as well as of physical quantities and their measurement, is the systematic study and quantification of the spatial and temporal distribution of absorbed energy in irradiated matter.

2.2.1 Definition of LET

The traditional approach to characterize the energy lost by charged particles along their track is based on the calculation of the collision stopping power, which is the mean rate of energy loss by the primary particle in interactions with orbital electrons, given by the Bethe-Bloch relation:

$$S = -\frac{d\,E}{dx} = \left(\frac{N_A\, e^4}{4\,\pi\, m_e\, \epsilon_0^2}\right) \cdot \rho\, \frac{z^2\, Z}{A\, v^2} \left[ln\left(\frac{2 m_e\, v^2}{I}\right) - ln(1-\beta^2) - \beta^2 \right] \qquad (2.1)$$

where z is the charge of the crossing particle, Z that of the medium matter, v the velocity of the impinging particle and I an empirical quantity indicating the mean energy required for ionizing a medium atom.
The stopping power, though, does not provide any information neither of the track structure nor of the statistical fluctuations of energy deposition in matter.

In 1952, Zirkle introduced the concept of Linear Energy Transfer (LET) as a descriptor of the radiation quality in order to highlight the fact that the knowledge of the energy absorbed by a medium is more relevant than the energy loss along the particle track. Moreover, it takes into account the difference between sparsely and densely ionizing radiation fields by adding to the absorbed energy the information of the path length of the deposition process (see Figure 2.3)
Following the definition given by ICRU [8], the linear energy transfer or restricted linear collision stopping power (L_Δ) of a charged particle in a medium is:

$$L_\Delta = \left(\frac{dE}{dl}\right)_\Delta \qquad (2.2)$$

where dl is the distance traversed by the particle and dE is the average energy locally imparted due to collisions with energy transfers less than some specified

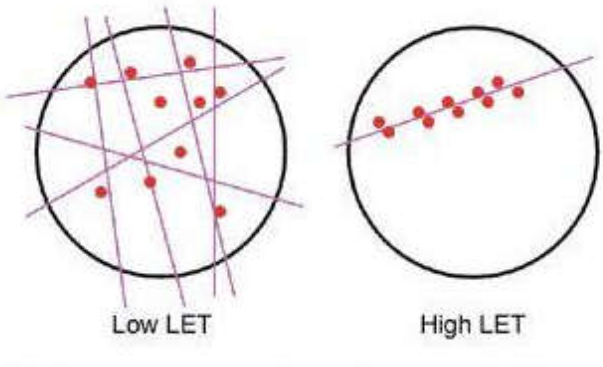

Figure 2.3: Illustrative sketch of the comparison between low- and high-LET radiation fields, distinguishing sparsely and densely ionizing radiation fields. See text fo details.

value Δ.

The term "locally imparted" may refer either to a maximum distance from the particle track or to a maximum value of discrete energy loss by the particle beyond which losses are no longer considered as local. High energy electrons (i.e. δ rays), in fact, may travel a certain distance from the track, carrying energy away from the target volume. In other words, if the site size is smaller than the maximum range of the δ rays, the energy lost by the incident particle is not fully absorbed in the volume of interest.

If no thresholds are applied, the simplest parameter to use is the unrestricted Linear Energy Transfer LET_∞, defined as the energy loss per unit distance of the charged particles originally set in motion by electromagnetic radiation or neutrons, or of the charged particles which originate in radiation sources. LET_∞, which includes all possible energy transfers, is equal to the collision stopping power.

By definition, LET is an average quantity which does not take into account the random nature of the energy loss of a given particle along its track, which can result in great variations in energy deposition when considering small volumes. Therefore, at the micro- and nano-metric scale, it is necessary to consider measurable physical quantities that reflect the stochastic nature of the inchoate energy deposition.

2.2.2 Definition of Microdosimetric Quantities

To overcome the limitations imposed by the LET concept, in 1959 Harald Rossi proposed a new methodological approach based on a set of stochastic quantities for the description of the energy-deposition events in microscopic structures, namely microdosimetry [9].
The term 'microdosimetry' refers to "a conceptual framework and corresponding experimental methods for the systematic analysis of the microscopic distribution of energy deposition in irradiated matter". The objective is "to develop concepts which relate some of the principal features of the absorption of ionizing radiation in matter to the size and perhaps the nature of the structure being affected" (International Commission on Radiation Units and Measurements, ICRU report 36).

The discrete interactions of ionizing radiation with matter occur in the so-called transfer points, where fraction of the energy imparted is absorbed.
In the microdosimetric approach, the fundamental quantity is the energy deposit ϵ_i which was introduced for the description of the spatial distribution of energy in charged-particle tracks. ϵ_i, which has not to be confused with the energy expended by the crossing particle, is defined as the energy deposited at a transfer energy point i:

$$\epsilon_i = T_{in} - T_{out} + Q_{\Delta m} \tag{2.3}$$

where T_{in} and T_{out} are the kinetic energies of the incident ionizing particle and the sum of the kinetic energies of all ionizing particles leaving the transfer point (excluding the rest mass), respectively. $Q_{\Delta m}$ is the change of the rest mass energy of the nucleus and all particles involved in the interaction. The unit of ϵ_i is the Joule or eV.
The term 'ionizing particle' refers to directly, as well as to indirectly, ionizing radiations capable of creating a change in the irradiated matter due to single interactions. Because of the production of delta rays, only a fraction of the energy imparted by ionizing radiation is instrumental in causing changes and any effects resulting from them, and the transfer points where this fraction is absorbed will be termed relevant transfer points. The minimum energy required for the physical, chemical or biological change under consideration will be symbolized by ω and

transfer of energy in excess of ω will be termed a significant energy deposit at a significant transfer point. A significant transfer point becomes therefore relevant if a change occurred, where the term 'change' refers to alterations that may be due to different mechanisms (if the change under consideration is ionization in a polyatomic gas, it requires energy transfers that vary among atoms and their electronic shells and ω is equal to the lowest ionization potential). When $\epsilon_{j,max} < \omega$, i.e. the largest transfer is not significant, no relevant transfer points can be produced. Such particles are non-ionizing and their energy is considered locally absorbed rather than included in T_{out}.

The stochastic quantity energy imparted ϵ is the sum of all energy transfers within a defined volume, named site:

$$\epsilon = \sum_i \epsilon_i \tag{2.4}$$

where the summation is performed over all energy deposits in that volume, due to one or more energy deposition events.

The specific energy z is defined as the quotient of the imparted energy ϵ by the mass of the matter m in a given volume:

$$z = \frac{\epsilon}{m} \tag{2.5}$$

The unit of z is the joule per kilogram, namely the gray (Gy). It is a stochastic quantity and is characterized by a probability density distribution $f(z)$.

Its expectation value, or mean specific energy, is a non-stochastic quantity and its limit as the mass volume approaches to zero coincides with the absorbed dose value D:

$$\overline{z} = \int_0^\infty z \cdot f(z)\, dz \tag{2.6}$$

$$\lim_{m \to 0} \overline{z} = D \tag{2.7}$$

For microscopic volumes and a large number of events, it is assumed that the specific energy is almost uniformly distributed in the site, therefore:

$$\overline{z} \simeq D \tag{2.8}$$

The lineal energy y is defined as the ratio between the imparted energy ϵ_s by a single event and the mean chord length $\bar{l}$ of the cavity:

$$y = \frac{\epsilon_s}{\bar{l}} \tag{2.9}$$

The unit of y is the Joule per meter or, most commonly, the keV$\cdot\mu$m^{-1}. The lineal energy is a stochastic quantity described by the probability density distribution $f(y)$. It is the stochastic analogous to the LET quantity, with the difference that LET disregards the energy-loss straggling, the angular scattering and the contribution of δ rays. For a convex volume, the mean chord length (defined as the mean length of randomly oriented chords in the volume), is given by Cauchy's theorem [10]:

$$\bar{l} = \frac{4V}{A} \tag{2.10}$$

being A the surface area of the volume V.
For a spherical volume, as for a right cylinder, the relation between the mean chord length $\bar{l}$ and the diameter d of the cavity is the following:

$$\bar{l} = \frac{2}{3}\, d \tag{2.11}$$

It is important to stress that lineal energy is defined for only single energy-deposition events, i.e. events that are caused by a single particle and its secondaries only.

The single event distribution is denoted by:

$$f(y) = \frac{d\,F(y)}{dy} \tag{2.12}$$

where $F(y)$ is the distribution of lineal energy less or equal to y and $f(y)$ is the frequency probability density, which represents the probability of having one event with lineal energy within the interval $(y, y + dy)$.
It is also useful to consider the dose distribution $D(y)$ of lineal energy, defined as the fraction of absorbed dose with lineal energy less or equal to y. The dose

probability density is defined as:

$$d(y) = \frac{d\,D(y)}{dy} \tag{2.13}$$

By definitions, the probability density functions (see Figure 2.4) are normalized to unity:

$$\int_0^\infty f(y)\,dy = 1 = \int_0^\infty d(y)\,dy \tag{2.14}$$

The first moment of the $f(y)$ distribution is the frequency-mean lineal energy:

$$\overline{y}_F = \int_0^\infty y \cdot f(y)\,dy \tag{2.15}$$

The relation between the dose and frequency probability densities is:

$$d(y) = \frac{y \cdot f(y)}{\overline{y}_F} = \frac{y \cdot f(y)}{\int_0^\infty y \cdot f(y)\,dy} \tag{2.16}$$

The second moment of the $f(y)$ distribution is the dose-mean lineal energy:

$$\overline{y}_D = \int_0^\infty y \cdot f(y)\,dy = \frac{1}{\overline{y}_F}\int_0^\infty y^2 \cdot f(y)\,dy \tag{2.17}$$

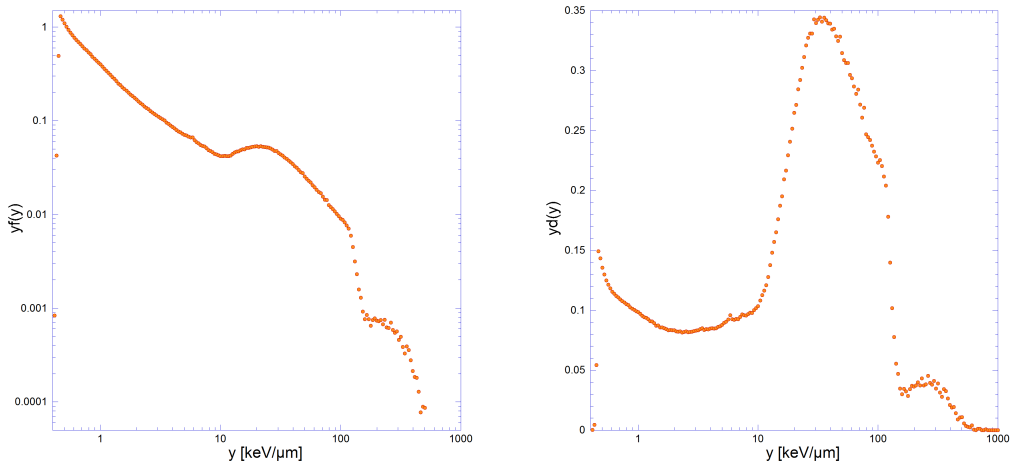

Figure 2.4: Frequency (normalized counts) and dose distributions for a neutron source, as a function of the lineal energy.

Similarly, probability distributions and average quantities are also defined for the specific energy: z is a stochastic quantity, but it can represent the sum of energy imparted by more than one event, therefore a subscript 1 is used to indicate the single-event probability density $f_1(z)$.

Since most distributions of lineal energy span over several orders of magnitude, microdosimetric spectra are usually displayed in a semi-logarithmic representation. In order to preserve the probabilistic meaning of the areas displayed in the spectra, which allows to compare spectra of different types of radiation, a $y \cdot f(y)$ versus $log(y)$ representation is adopted. Similarly, dose distributions are plotted by using a $y \cdot d(y)$ versus $log(y)$ representation: the area under the curve between two y values results proportional to the fraction of dose delivered by events with lineal energies in the range considered, or, in other words, equal subtended areas correspond to equal dose contributions.

2.2.3 The Radiobiological Weighting Function

The microdosimetric distributions provide information about the radiation quality that can be useful to estimate the biological effectiveness of a given radiation modality. A method for assessing the beam quality in terms of the relative biological effectiveness (RBE) was proposed by Wambersie [11], who introduced an empirical biological weighting function $r(y)$ (see Figure 2.5) to fold the single-event microdosimetric distribution $d(y)$ by following the relation:

$$RBE = \int_0^\infty r(y) \cdot d(y)\, dy \tag{2.18}$$

where the RBE is obtained from radiobiological measurements and $d(y)$ derives from microdosimetric measurements. In this way, $r(y)$ can be obtained by unfolding the previous equation after performing in parallel both radiobiological and microdosimetric measurements for the same radiation field [12] [13].

As already mentioned, the weighting function is not univocal, because radiobiological data strongly depend on several factors such as the cell type, the biological end-point, the beam characteristics, the absorbed dose, the absorbed dose rate, the physiological conditions of cell cultures and so on, and its value strongly depends on the conditions at which it has been evaluated.

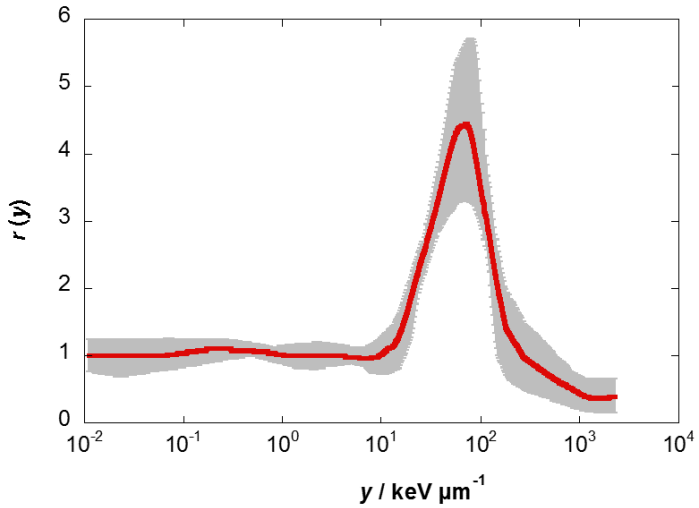

Figure 2.5: Biological weighting function $r(y)$ for intestinal crypt cells regeneration in mice for 8 Gy derived from neutron therapy beams (thick line). The grey area corresponds to ± 1 standard deviation [Pihet et al., 1990].

2.2.4 Experimental Methods and Limits in Microdosimetry

Microdosimetric measurements consist in evaluating experimental quantities closely related to the imparted energy.

An ideal detector to be applied should fulfill the following criteria:

- It should be usable for determining the distribution over a sufficiently large range of volume sizes;
- The entire range of energy imparted should be measurable;
- The signal from the detector should be proportional to energy imparted;
- The detector signal formed by the smallest energy imparted should be free from any fluctuations due to the detector itself.

Neither a detection nor a simulation principle which can fulfill all of these conditions does exist. Compromises that have to be accepted impose limitations on the accuracy of experimentally determined distributions of energy imparted.

Among the various detection and simulation methods suggested in the literature, gas-filled detectors have been mostly used by exploiting the principle of simulation of a micrometric volume of tissue (in the range of the diameter of a cell nucleus). That is achieved by replacing the volume with a larger cavity filled with a tissue equivalent gas of lower density (see section 3.1) [6]. The proportional counters employed in microdosimetry are walled or wall-less detectors filled

with tissue-equivalent gases (generally propane-based or methane-based).
Tissue Equivalent Proportional Counters (TEPCs) are the reference microdosimetric walled devices, consisting in a spherical or a cylindrical volume with a central anode wire electrically isolated from the surrounding walls. The quality of a microdosimetric measurement performed with a TEPC strongly depends on the atomic composition and on the pressure stability of the filling gas. The best way of ensuring constant composition and pressure is to employ a gas flow system.
Wall-less TEPCs have been developed in order to minimize the so-called 'wall effects', the distortion of the measured signal due to the higher density of the counter wall with respect to the gas filling the cavity. This effect results in a higher energy deposition in the sensitive volume caused by additional particle tracks generated by scattering events, introducing errors estimated to be of the order of 10%. The sensitive volume of wall-less TEPCs is defined through a grid with a high transparency ratio, which acts as a cathode.

TEPCs are characterized by an optimum tissue-equivalence, and their response to primary and secondary charged particles is accurate over a wide energy range. For microdosimetry of hadron therapy fields, the development of miniaturized counters, named mini-TEPCs, allows to improve the physical description of treatment fields, and therefore to increase the accuracy of the treatment itself [14] [15]. This technique can measure not only the usual dose distributions, but also the local fluctuations of the imparted energy, which can be useful for a more comprehensive knowledge of the physical process leading to the biological effects.
Such microdosimeters have already shown to properly assess the RBE of the radiation by linking the physical parameters of the radiation. By combining microdosimetric measurements of energy deposition with the corresponding biological response and radiobiological data, weighting functions are extracted with enough accuracy in order to monitor the therapeutic beam biological effectiveness [16]. Nevertheless, at present it is not possible to characterize the RBE by using the microdosimetric distributions only, since empirical weighting functions are still necessary. Moreover, the microdosimetric spectrum depends on the sim-

ulated site size, even when the reference biological effect may be the same. As a consequence, the weighting function is not unique, as already mentioned, but it changes as a function of the size of the simulated site (as well as the absorbed dose, the absorbed dose rate, the biological end-point, the radiation field and so on).

The biological damage induced by radiation is known to start with injuries to sub-cellular structures, such as the chromatin fibers and the DNA segments, and the damage is strictly related to the track structure of ionizing radiation playing a significant role at the nanometer level [17].
The microdosimetric approach, based on the local energy imparted to sensitive volumes of matter at micrometer length scale, can not give detailed information about that [18]. On the contrary, track-nanodosimetry completes the physical description of radiation-cell interaction since it properly extends to DNA-size sites, smaller than the inter-track ionisation structure, the experimental investigation [19].
However, both the physical quantities and the experimental tools used in track-nanodosimetry are different from those ones used in microdosimetry.

2.3 Fundamentals of Track-Nanodosimetry

The complexity of the damage and its repairability are likely to be related to the properties of the ionizing radiation track structure within critical sites, having sizes from a few to a few tens of nanometers.

It is generally accepted, thanks to recent radiobiological data, that the effects of ionizing radiation on living systems start with damages to the sub-cellular structures, such as DNA structure, either directly or indirectly [20].
In the first case, radiation interacts with the atoms of the DNA molecule, or some other cellular component critical for the survival or the reproduction of the cell. The indirect effect arises from the interaction of radiation with the water molecules, which constitute most of the cells volume: the production of frag-

ments, such as hydrogen and hydroxyls, can recombine or interact with other fragments or ions and form toxic compounds, such as hydrogen peroxide, which can contribute to the destruction of the cell.

An isolated damage to the DNA structure, named a single strand break (SSB), has a high probability of repair, since the opposite strand remains intact. On the contrary, a double strand break (DSB), being difficult to repair, may cause the death of the cell [1] [21]. A clustered damage, composed of multiple DSB very close to each other and likely to affect the nitrogen-containing bases of the DNA, has a high probability of causing the death of the cell. Figure 2.6 schematically shows the different types of possible damages to the DNA molecules.

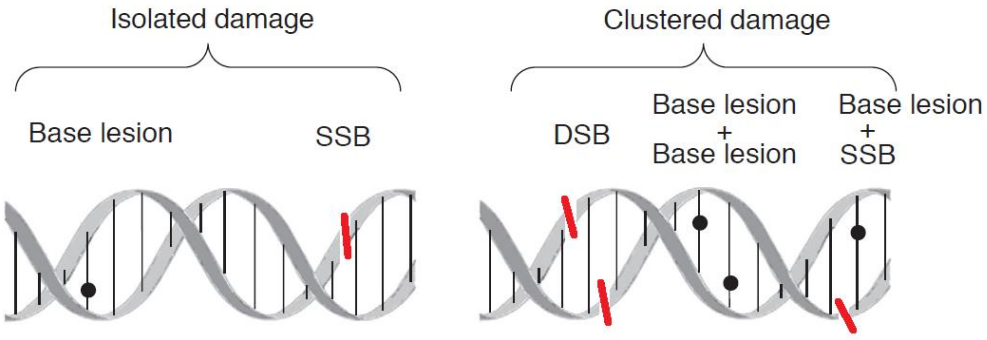

Figure 2.6: Sketch of the possible damages to the DNA molecules: isolated damage (base lesion or SSB) and clustered damages (more lesions one close to the other and DSB).

2.3.1 Experimental Nanodosimetry

Track-nanodosimetry studies the characteristics of the particle track structure that can be relevant for induction of initial radiation damage. In particular, it aims to give a theoretical and experimental description of ionization fluctuations occurring in a nanometric site placed at different impact parameters from the particle trajectory [22] [23] [24].

The track structure description is given in terms of the frequency distributions of the number of ionizations occurred in the sensitive volume per single primary particle. The number of ionizations includes those produced in interactions of secondary electrons within the site, and it is a stochastic quantity defined as

"ionization cluster size ν".

The idea is simple: a sensitive volume is placed at a specific impact parameter d with respect to the particle beam direction, and the number ν of ionizations occurring inside the sensitive volume at each particle passage is counted (see Figure 2.7).

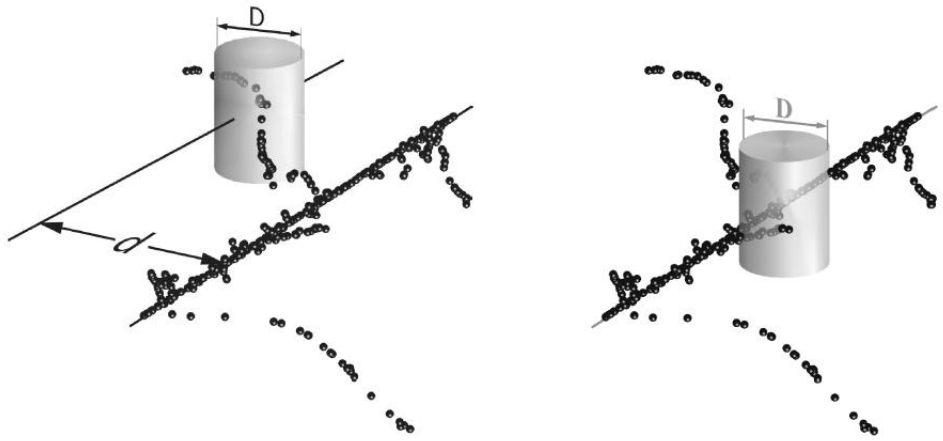

Figure 2.7: Simulation of ionization clusters generated by a primary particle passing a given cylindrical volume of size D: the particle trajectory may cross the volume (impact parameter d = 0, on the right) or pass at a distance d from the cylinder (on the left) [22].

By repeating the measurements for a high number of primary particles, the frequency distribution P_ν(Q, d, D) can be interpreted as the probability that exactly ν ionizations are produced within a given cylindrical target volume of size D placed at an impact parameter d with respect to the trajectory of a single primary particle of radiation quality Q, meaning particle type and energy. Figure 2.8 shows an example of measured P_ν distributions for different radiation qualities at an impact parameter d = 0

The k-th moment M_k(Q, d, D) of the distribution is defined as:

$$M_k(Q,d,D) = \sum_{\nu=1}^{\infty} \nu^k \, P_\nu(Q,d,D) \tag{2.19}$$

The mean ionization cluster size in the target volume is given by the first moment,

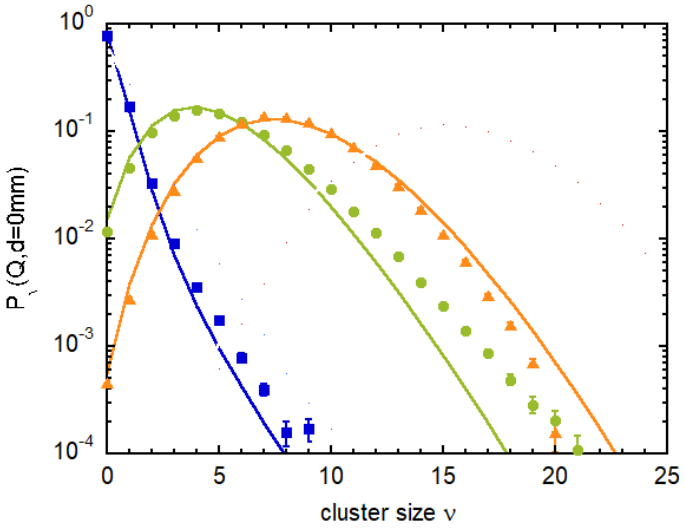

Figure 2.8: Cluster size distributions P_ν(Q, d= 0, D) obtained with the StarTrack counter for different radiation beams: 20 MeV p (squares), 48 MeV ^{6}Li (circles) and 240 MeV ^{12}C (triangles). See text for details [24].

i.e. $M_k(Q, d, D)$ for $k = 1$:

$$M_1(Q, d, D) = \sum_{\nu=1}^{\infty} \nu \, P_\nu(Q, d, D) \tag{2.20}$$

The cumulative probability of forming ionization cluster sizes $\nu \geq \zeta$ is given by the following sum distribution:

$$F_\zeta(Q, d, D) = \sum_{\nu=\zeta}^{\infty} P_\nu(Q, d, D) \tag{2.21}$$

From the radiobiological point of view, if the nanometer target simulates the DNA molecule, the complexity of the biological damage is intuitively proportional to the cluster size. Recent data [25] demonstrated that when plotting the cumulative probabilities F_1 , F_2 and F_3 as a function of M_1, all the experimental points fall on an almost unique curve, independent of the detector used and the site size: the measured value of M_1 uniquely determines F_k up to $k = 3$, no matter how M_1 is obtained, by changing either the radiation quality or the size of the target volume (see Figure 2.9). Moreover, a deep correlation between the cumulative distributions and the biological inactivation cross-sections was found. In particular, a direct proportionality between the F_2(Q,d= 0,D= 1 nm) cumulative distribution and the $\sigma_{5\%}$ cross section, and between the F_3(Q,d= 0,D= 1.5 nm)

and the σ_α have been highlighted, where $\sigma_{5\%}$ and σ_α indicate the cellular inactivation cross sections calculated at 5% survival and at initial survival, respectively (see Figure 2.10).

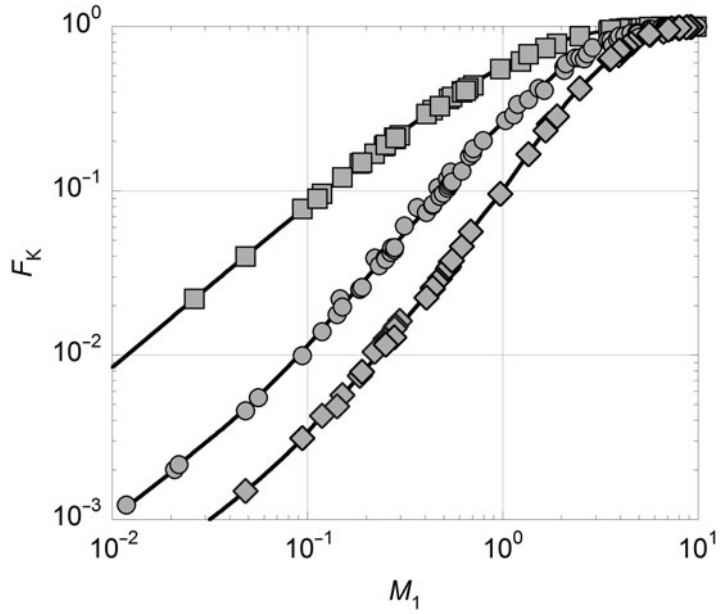

Figure 2.9: The cumulative distributions F_1 (upper), F_2 (middle) and F_3 (lower) as a function of the mean cluster size M_1, for several radiation qualities and several site sizes (see [25]).

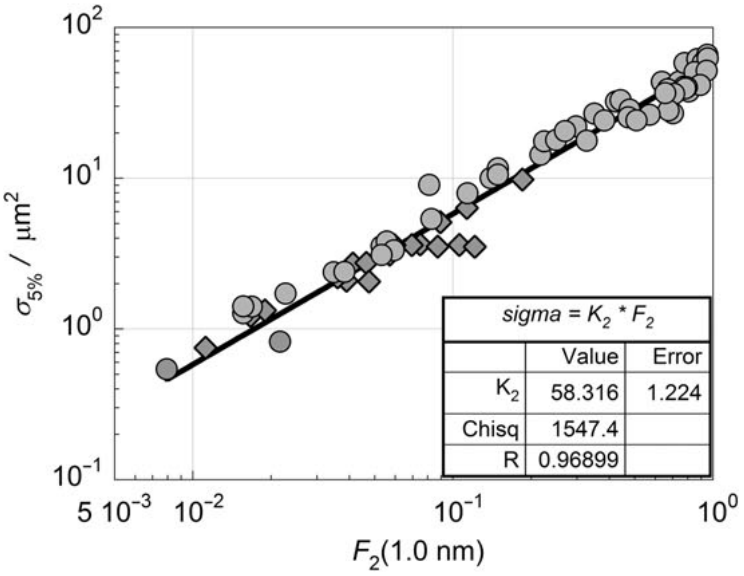

Figure 2.10: Inactivation cross sections at 5% survival for V79 cells (chinese hamster) irradiated with protons (diamonds) and carbon-ions (circles), plotted as a function of the nanodosimetric F_2(Q,d= 0,D= 1 nm). The line is the least-squares best fit to experimental data (see [25]).

Nanodosimetry is performed by filling a small volume with a low-density gas in order to simulate nanometric structures and by counting the number of electrons or positive ions produced event by event in the volume itself by the imping particle. A typical target volume is a cylinder with the dimensions of a DNA segment 10 base pairs in length, i.e. from 2 to 4 nm in height and diameter, and usually it is assumed that the cylinder is filled and surrounded by water
Similarly to microdosimetry, nanodosimetry is based on a density scaling principle to simulate target volumes of different sizes and compositions.

At present, three types of nanodosimeter devices have been developed: the StarTrack counter of the Legnaro National Laboratories of the Italian National Institute for Nuclear Physics (INFN-LNL, Padova, Italy), which is a single-electron counter; The Jet Counter of the Polish National Center of Nuclear Research (NCBJ, Otwock- wierk, Poland), which measures positive ions produced by the primary particle in a pulsed jet of nitrogen gas propagating inside a cylindrical tube; The Ion Counter of the German National Metrology Institute (PTB, Braunschweig, Germany) detects positive ions produced in a wall-less gas volume. They vary in the detected particle type, the operating gas and the size of the equivalent nanometric target in biological matter.
In particuar, the StarTrack detector of the Legnaro National Laboratories is able to measure cluster-size distributions in a wall-less nanometric volume placed at different impact parameters from the ion path [26]. The target volume, a cylinder 3.7 mm in diameter and height, is filled with gaseous propane at a density of $5.47 \mu g\,cm^{-3}$ which corresponds to a mass per area of about $2 \mu g\,cm^{-2}$. Hence, at a density of $1\,g\,cm^{-3}$, the target volume is comparable in size to a segment of chromatin fiber 20 nm in diameter and height. The target volume can be moved perpendicularly to the central axis of a narrow particle beam with 0.1 mm accuracy, allowing to measure at different impact parameters. When the ion path is outside the sensitive volume, the counter measures inside the so-called penumbra, which is the space region where events are due to only long-range δ-rays. When the ion path passes through the sensitive volume, the counter measures inside the so-called track core, a space region where ionizations are due to both primary ions and their secondary electrons.

2.4 A Bridge Between Microdosimetry and Track-Nanodosimetry

As explained in the previous sections, microdosimetry measures the statistical fluctuations of the local energy imparted at the micrometer level by deriving the single- event distribution of energy imparted. The tissue equivalent proportional counter is the most accurate device to measure the microdosimetric properties of a particle beam, and it is able to simulate site sizes in the micrometric domain. At present, transportable devices are available, allowing to characterize unknown radiation fields. Nevertheless, since the lower operation limit of the common TEPCs is about 300 nm [27], no detailed information on the track structure can be obtained.

On the other hand, the pattern of particle interactions at the nanometer level is measured by track-nanodosimetry, which derives the single-event distribution of ionization cluster size for site dimensions from a few nanometers up to tens of nanometers. Nanodosimetric quantities behave similarly to radiation-induced damages to the DNA and are directly measured by only three different nanodosimeters worldwide. Nevertheless, practical instruments are not yet available. The gap between the microdosimetric and track-nanodosimetric results, that is at the same time a technological and a knowledge gap, could be partially filled by extending the TEPC performances down to the nanometric region. The microdosimetric spectra measured by such a device, in fact, would consist in the convolution of core and penumbra events, the two components of a particle track measured through a nanodosimeter. A prototype of this kind of TEPC demonstrated to properly work in the nanometric domain under various radiation fields [37], its physical response still being affected by the stochastics of the avalanche formation and having to be integrated with empirical radiobiological weighting functions, though.

The final aim of a direct comparison between microdosimetric spectra and track-nanodosimetric distributions for the same particle beam could allow to investigate the possibility of unfolding the microdosimetric spectrum into its different track components. In other words, the possibility of studying and performing

an innovative approach to the description of the radiation interaction with tissue at local level could be investigated.

For this purpose, a novel partially wall-less avalanche-confinement low pressure gas TEPC, able to simulate biological sites down to the nanometric region, has been designed, assembled and characterized.

Chapter 3

Experimental Microdosimetry with TEPCs

The Tissue Equivalent Proportional Counter (TEPC) is a spherical or cylindrical chamber constituted by tissue equivalent walls and filled with low density tissue equivalent gas. It operates in pulse mode: each ionization event traversing or occurring in the sensitive volume gives rise to a signal pulse. The collected pulse height spectrum provides the ionization distribution of charged particles that interacted with the detector.

3.1 The Principle of Simulation

TEPCs are commonly assumed to measure the distributions of energy imparted in micrometric volumes of tissue when irradiated by ionizing radiation.
In order to properly simulate a biological target, it is required that the energy loss of passing charged particles is identical in the tissue sphere and the gas sphere for equivalent trajectories. Practically, the elemental composition of the walls and of the filling gas of the TEPC should be as close as possible to that of tissue. The energy released in a medium only depends on its atomic composition, but does not depend on its chemical structure. For this reason, it is possible to exploit materials composed by mixtures that contain mainly H, C, O and N atoms [28]. Since the human tissue is not uniform (regions with different compositions and densities), the International Commission on Radiation Units and Measurements

(ICRU) defined a standard tissue to be used as a reference, called ICRU muscular tissue, whose elemental composition is reported in Table 3.1.

The most frequently used tissue equivalent mixtures are methane-based TE (64.4% CH_4, 32.4% CO_2 and 3.2% N_2) and propane-based TE (55% C_3 H_8, 39.6% CO_2 and 5.4% N_2) gases. Recently also dimethyl ether has been exploited as filling gas for TEPCs (DME: $(CH_3)_2O$), which can be considered as a tissue-equivalent gas apart from the lack of nitrogen.

The detector walls are generally fabricated with tissue-equivalent conducting plastics (A-150 Shonka): they show a higher amount of carbon with respect to the ICRU muscular tissue, in order to guarantee good conducting characteristics, since they act as the detector cathode [29].

Material	H	C	N	O	Na	Mg	P	S	K	Ca	F
Tissue ICRU	10.2	12.3	3.5	72.9	0.08	0.08	0.2	0.5	0.3	0.01	-
Shonka A-150	10.1	77.6	3.5	5.2	-	-	-	-	-	1.8	1.7
CH_4 - TE	10.2	45.6	3.5	40.7	-	-	-	-	-	-	-
C_3 H_8 - TE	10.3	56.9	3.5	29.3	-	-	-	-	-	-	-
DME + N_2	12.5	50.2	3.5	33.8	-	-	-	-	-	-	-

Table 3.1: Elemental composition of muscular tissue equivalent compounds and tissue substitutes in percentage by weight.

The simulation of tissue sites is based on the concept of equal energy released in the gas cavity and in the microscopic volume of tissue. The principle of simulation, in fact, states that a micrometric volume of tissue is equivalent to a macroscopic volume of gas if the energy loss of passing charged particles is identical in the tissue sphere and the gas sphere for equivalent trajectories.

$$\Delta E_{tissue} = \Delta E_{gas} \tag{3.1}$$

Taking into account the mass stopping powers, the same equation can be rewritten in:

$$\left(\frac{1}{\varrho}\frac{dE}{dx}\right)_t \varrho_t d_t = \left(\frac{1}{\varrho}\frac{dE}{dx}\right)_g \varrho_g d_g \tag{3.2}$$

where $\left(\frac{1}{\varrho}\frac{dE}{dx}\right)$ is the mass stopping power in tissue (t) and in gas (g), ϱ is the density of the tissue (t) and of the gas (g) and d is the diameter of the tissue site to simulate (t) and the diameter of the sensitive volume of the gas detector (g).

The simulation is done by replacing the simulated site ($10^1 - 10^2$ nm) with a larger cavity ($10^0 - 10^1$ mm) filled with a tissue-equivalent gas, by properly adjusting its density.

Fano's theorem states that in a medium of constant atomic composition, the fluence of secondary particles is constant if the fluence of primary particles is constant and that under this condition, the fluence is independent of the density variations, provided the interaction cross section and stopping powers of the particles are independent of density [30]. If the atomic composition of tissue and gas are identical, and if the mass stopping powers are independent of the density, the stopping powers are assumed to be equal for the radiation under consideration and the principle of simulation reduces to the relationship:

$$\varrho_g = \varrho_t \frac{d_t}{d_g} \tag{3.3}$$

where ρ_g is the gas density, d_t the diameter of the tissue site one wants to simulate, the tissue density ϱ_t is assumed to be equal to $1g \cdot cm^{-3}$ and the diameter of the detector sensitive volume d_g is fixed.

Once the gas density ϱ_g is obtained, the corresponding gas pressure P_g inside the cavity of diameter d_g can be obtained from the ideal gas law:

$$P_g = P_0 \frac{\varrho_g}{\varrho_0} \frac{T_g}{T_0} = \varrho_t \frac{d_t}{d_g} \frac{1}{\varrho_0} \frac{P_0 T_g}{T_0} \tag{3.4}$$

where ϱ_0 is the gas density at standard pressure ($P_0 = 101325\,\mathrm{Pa}$) and standard temperature ($T_0 = 273.15\,\mathrm{K}$) and T_g is the actual temperature.

3.2 The Electronic Avalanche and the Gas Gain G

Proportional counters usually consist of two electrodes, a central anode surrounded by a conductive wall that acts as a cathode. These detectors, operating in pulse mode, provide an electrical signal which is proportional to the number of ion pairs resulting from an energy-deposition event, linearly amplified in magnitude by gas multiplication if a sufficiently high electrical field is applied between

the electrodes [31].

In particular, electrons generated in the ionization process of the gas molecules by the radiation field, drift towards the anode wire under the effect of the voltage difference between the electrodes and gain kinetic energy. If this energy is greater than the ionization energy of the neutral gas molecule, primary electrons may act as further ionizers and generate secondary electrons. This process leads to an avalanche multiplication, known as a Townsend avalanche, which results in a larger pulse at the output. The fractional increase in the number of electrons per unit path length dx is given by the Townsend equation:

$$dn = \alpha_T \, n \, dx \tag{3.5}$$

where α_T is the first Townsend ionization coefficient for the gas, defined as the mean number of electrons produced per unit path length by a single primary electron in the direction of the electric field. By definition, it is the reciprocal of the mean free path per ionization λ_{ion} [32]:

$$\alpha_T = \frac{1}{\lambda_{ion}} \tag{3.6}$$

α_T depends on what has been termed the 'reduced field strength', $\frac{E}{P}$ (P = gas pressure) and it is equal to zero for reduced electric field strength lower than a given threshold, which corresponds to the production of a secondary ion pair.

Thanks to this multiplication process, the ionization from a primary particle which interacts with the detector sensitive volume gives rise to a measurable signal, large enough to be distinguished from the electronic noise. The total number of electrons collected at the anode wire N_c is proportional to the number of primary electrons N_g produced in the sensitive volume by the initial radiation by a factor G, called gas gain.

$$G = \frac{N_c}{N_g} \tag{3.7}$$

The voltage difference between the anode wire and the cathode $\Delta V_{a-c} = V_a - V_c$ is chosen in order to assure the proportionality between N_c and N_g (detector operation in the so-called proportional region).

Proportional counters are usually cylindrical or spherical, because the application of very high electric fields is needed to start the electronic avalanche: with respect to a parallel plate geometry, a lower voltage difference between the electrodes is required to achieve the same electric field strength. Despite the isotropic response of the spherical detectors, cylindrical counters are preferred because of their construction and design: in fact, the radial field symmetry shows a more uniform electric field around the wire.
The electric field $E(r)$ in a cylindrical geometry along the radial distance r is given by the following relation:

$$E(r) = \frac{V_a - V_c}{r\, ln\left(\frac{r_c}{r_a}\right)} = \frac{K}{r} \tag{3.8}$$

where V_a and V_c are the applied voltage to the anode and cathode respectively, r_a and r_c are the radii of the anode wire and the cathode, $K = \frac{V_a - V_c}{ln\left(\frac{r_c}{r_a}\right)}$ is a factor which depends only on the size of the counter and the applied voltages.

The sensitive volume between the anode wire and the cathode wall can be subdivided in two different operating regions:

- drift zone: the primary electrons, generated by the ionization events due to the interaction between radiation and gas molecules, move towards the anode wire without any further ionization. No multiplication occurs in this region;
- multiplication zone: in the vicinity of the anode wire, the drifted electrons have enough energy to induce additional ionization events, which produce further electron-ion pairs. This phenomenon, named electronic avalanche, occurs if a high enough electric potential is established between the anode wire and the cathode.

The multiplication factor G, the mean number of electrons collected at the central wire per primary ion pair produced by the ionizing particle, can be expressed in terms of the first Townsend ionization coefficient α_T. For cylindrical proportional counters with anode and cathode radii r_a and r_b, respectively, the numerical value

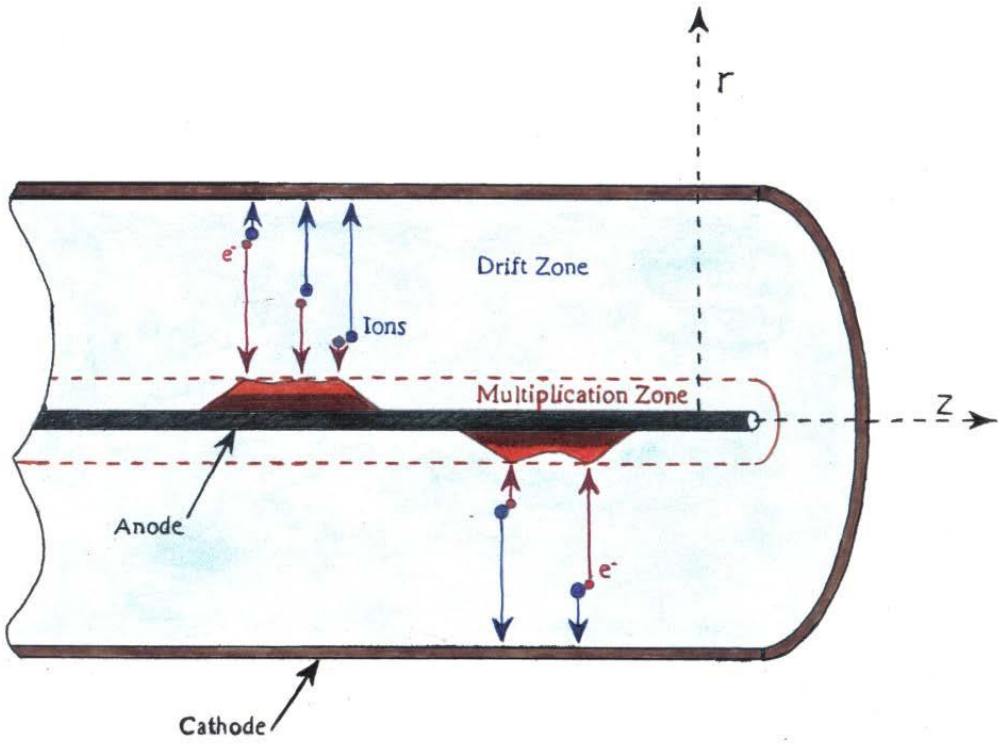

Figure 3.1: Sketch of the drift and multiplication regions in a cylindrical proportional counter [33].

G of the gas gain can be evaluated using the expression:

$$ln(G) = \int_{r_a}^{r_c} \alpha_T(r)\, dr \tag{3.9}$$

When the proportional counter is properly working, the electronic avalanche occupies only a portion of the whole sensitive volume, as shown in Figure 3.1 since no multiplication occurs in the drift zone. Thus, the contribution of the drift zone to the integral is null and the upper integration limit r_c can be substituted by r_m, which is the critical radius beyond which $\alpha(r)$ is 0, meaning that the electric field is too weak to generate secondary electrons, thus starting the avalanche. Therefore, the multiplication factor is obtained by integrating the first Townsend ionization coefficient α_T over the multiplication zone which depends on the critical radius r_m, on the nature of the gas, on its pressure P_g and on the applied electric field strength E through the 'reduced field strength', $\frac{E}{P}$.

The number of electrons collected by the anode per initial ion pair is not constant, but is a statistical variable. The stochastic process of gas multiplication, introducing a fluctuation, broadens the measured number spectra of initial ion

pairs. Moreover, a definite extension of the multiplication zone is one of the most crucial factors to determine the limits of the energy resolution of a counter: primary ionizations which occur within the multiplication region will produce signals whose amplitude depends on the interaction position inside this zone. This phenomenon produces a further variance to the ionization statistics. In order to achieve a uniform multiplication for all the primary electrons generated by the interaction between radiation and gas molecules and reduce this further variance, it is required that this interaction occurs in the drift zone only. For these reasons, the ideal counter should show a multiplication region as small as possible if compared to the total sensitive volume [34].

Once the multiplication factor G is well established, it is possible to determine the number of electron-ion pairs generated in the gas.
In fact, the physical quantity actually measured by proportional counters employed in microdosimetry is a charge that is proportional to the number of ion pairs created by traversing particles, the so called W-value. It provides a quantitative correlation between the number of ion pairs created and energy imparted and can be used to convert the measured ionization spectrum into a spectrum of energy imparted.
The W-value depends on the type of gas, the type of ionizing radiation and its energy is defined as the quotient:

$$W = \frac{E}{N} \tag{3.10}$$

where N is the mean number of electron-ion pairs generated by an initial ionization particle with kinetic energy E completely dissipated in the gas [35].
Since the particle loses its energy in the gas by both ionization and excitation events, the W-value results greater than the ionization potential I of the gas. For a given energy, it increases with particle mass; for a given mass, it decreases with particle energy. A constant W-value is usually applied for the entire spectrum, thus introducing errors in the spectra of energy imparted. Another basic limitation of the ionization measurement is the fact that the lowest charge detectable is that corresponding to a single ion pair.

3.3 Avalanche-Confinement TEPCs

The site sizes of interest in microdosimetry are at the micrometric scale, with an upper limit given by the average cell diameter equal to about $10\,\mu$m. The common TEPCs, which are nowadays commercial, are designed in order to measure single event spectra in sites $100 - 200\,\mu\text{g}\cdot\text{cm}^{-2}$ in diameter, which correspond to diameters of $1 - 2\,\mu$m at a density of $1\ \text{g}\cdot\text{cm}^{-3}$. Nevertheless, the results obtained by this technique are not sufficient to have a complete information about the biological effectiveness of ionizing radiation, since the biological damage induced by radiation starts with injuries to sub-cellular structures, such as the chromosomes or the DNA: the cell damage is strictly related to the spatial distribution of the interaction points between the charged particle and matter.

For this reason, it is necessary to study the track structure of the interacting particle at nanometer level, where the site size is smaller than the ion track structure. Because of that, it would be useful to lower the TEPC active volume down to smaller dimensions in order to measure the fluctuations of the energy absorbed in nanometric sites. The lower limit of the operating range in experimental microdosimetry results equal to about 300 nm though, which is imposed by the excessive expansion of the electronic avalanche at very low pressures. This limit is based on several studies performed over tens of years: since the early 1970s, in fact, researchers have been interested in simulating sites of nanometric size for the interpretation of the radiobiological data which have proved that the radiation damage is initiated at the DNA level, as already mentioned.

Decreasing the gas pressure to simulate very small site sizes using conventional TEPCs leads to some technical issues: in fact, by decreasing gas pressure while keeping the same applied voltage (that is by decreasing the simulated site size), the number of ionizations generated in the sensitive volume decreases. Consequently, the amplitude of the signal from the TEPC becomes too low to be detected. The unique solution is to increase the gas gain of the TEPC in order to be able to measure single events, that means to produce a detectable signal over the noise threshold. Nevertheless, any attempt to increment the gas gain, by increasing the applied voltages at the electrodes, leads to a significant enlargement

of the electronic avalanche, which ultimately occupies the whole sensitive volume with an unacceptable loss of energy resolution.

A possible way to overcome this problem is to confine the electronic avalanche by exploiting a third electrode, represented by a helix which is co-axial to the anode wire. The voltage difference between the anode and the helix defines the size of the electronic avalanche region and, therefore, the gas gain. The region between the helix and the cathode is the electron drift region, in which the electrons move towards the avalanche region. The voltage difference between the cathode and the helix has to be high enough to avoid ion recombination and low enough to avoid charge multiplication. Once the primary electrons have crossed the helix, each one undergoes the same multiplication process regardless the actual position at which it was generated, thus minimizing the relative variance of the gas gain. This approach was adopted by Cesari et al., who designed an avalanche-confinement cylindrical TEPC filled with propane-based tissue equivalent gas mixtures and with dimethyl ether. This detector demonstrated to be able to work with a good energy resolution in the nanometric region, down to 50 nm when measuring with propane-based gas mixtures and down to 35 nm when using DME [36].

3.4 State of the Art: MiMi

As an improvement of the prototype developed by Cesari et al., a novel avalanche-confinement TEPC was recently built [37].

This detector, named MiMi (acronym for Microdosimetria Milano), was designed with the dimensions and the materials of the electrodes optimized in order to reach a higher gas gain at very low pressures, with the aim of studying the possibility of performing microdosimetric measurements down to 25 nm of simulated site size.

MiMi, whose picture and cross sectional view are displayed in Figure 3.2, consists of a cylindrical sensitive volume of 13 mm both in diameter and height and presents three different electrodes independently biased: a central anode wire (graphite, 1 mm in diameter), a cylindrical cathode shell (conductive plastic A-150 type, 13 mm in internal diameter and 1 mm in thickness) and a helix (gold-

plated tungsten, 100 μm in diameter) made of 19 coils, 6 mm in diameter, which surrounds the anode wire and subdivides the sensitive volume into the drift and the multiplication regions.

Two field tubes (stainless steel, 6 mm in diameter) are exploited to both sustain the helix and correctly define the sensitive volume, avoiding any distortions of the electric field, while two insulating Rexolite caps enclose the chamber. An orifice on the basis cap permits the gas inlet and outlet.

Two aligned holes were also designed in order to contain a thick removable ^{244}Cm alpha source, properly sealed by a mylar layer, and a very miniaturized solid state detector (SSD) which can work as a simple trigger or even as a spectrometer: a Osram BPX65 silicon photodiode with a 1 mm^2 active area has been selected for this application. This particular configuration is exploited for the determination of the electron transmission windows and the experimental gas gain of the TEPC. In such a way, only the signals due to alpha particles crossing the counter parallel to the anode wire were collected.

An external aluminum case (0.2 mm in thickness) is exploited for the containment and the protection of the chamber.

A cylindrical Rexolite layer (0.5 mm in thickness) is interposed between the cathode wall and the aluminum case to electrically isolate the latter.

Figure 3.2 shows a picture and a cross sectional view of the MiMi avalanche-confinement TEPC.

The MiMi detector demonstrated to properly work at simulated site sizes from 300 nm down to 25 nm corresponding to the range 13 mbar - 1 mbar in the gas pressure.

For each simulated size, an optimum range of voltage differences in the avalanche region ΔV_{a-h} and in the drift region ΔV_{h-c} was experimentally evaluated, thus determining the best working conditions of the detector.

The response of the device to photons emitted by a ^{137}Cs isotopic source and to fast neutrons was characterized experimentally at different simulated site sizes and configurations. The analysis of the microdosimetric spectra demonstrated the good performances of the device and the reproducibility of the calibration procedure.

Since the main objective of this doctoral project concerned the feasibility study

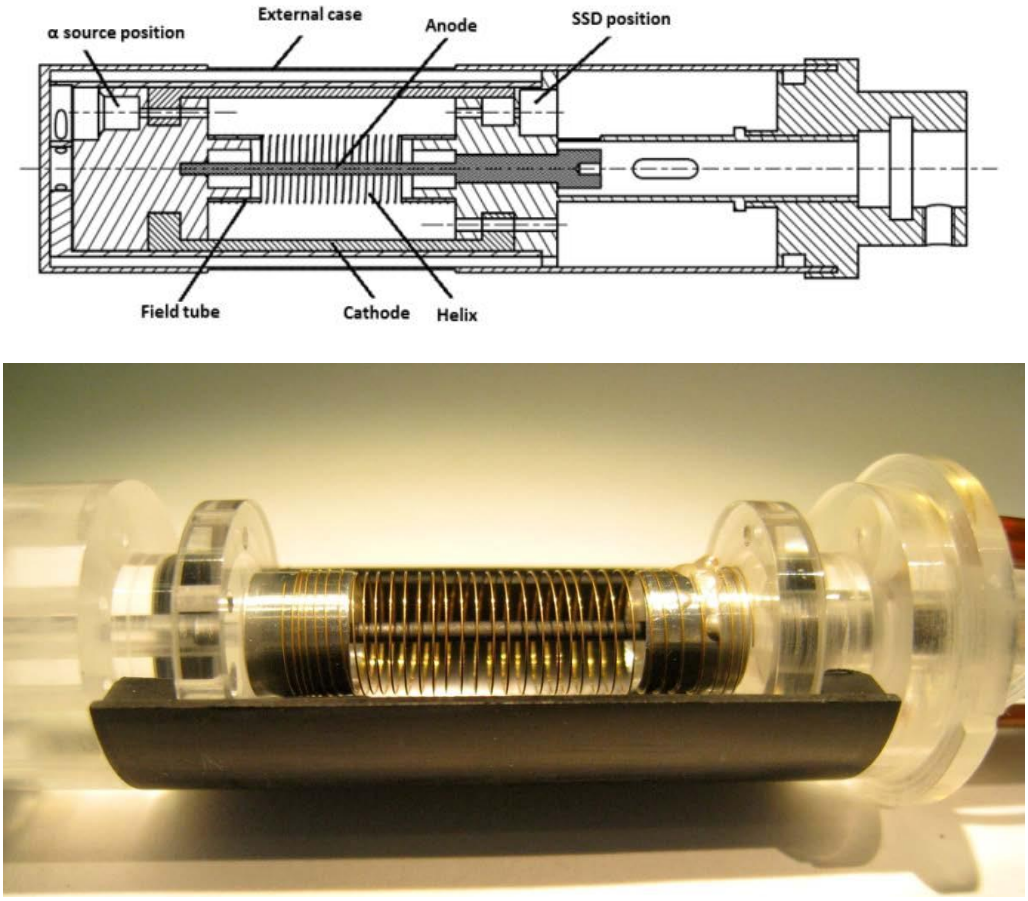

Figure 3.2: Cross sectional view (top) and picture (bottom) of the MiMi avalanche-confinement TEPC. The three independently biased electrodes and the positions of the alpha source and of the solid state detector are also indicated.

of a new type of TEPC which could fill the actual scientific gap between the approaches proposed by experimental microdosimetry and track-nanodosimetry for the physical characterization of hadron beams, the response of this novel avalanche-confinement TEPC to a low-energy carbon ion beam was experimentally evaluated. This irradiation campaign gave confidence about the capability of this novel avalanche- confinement TEPC of measuring in the range 300 nm - 25 nm when irradiated with low-energy carbon ions. It should be underlined that microdosimetric measurements of hadron beams at the nanometric scale with portable devices have never been performed before.

This detector is the actual prototype of the TEPC whose detection, assembly and first functional tests execution are discussed in this thesis.

As an example, Figure 3.3 and 3.4 show some energy and microdosimetric spectra obtained with the exploitation of Mimi.

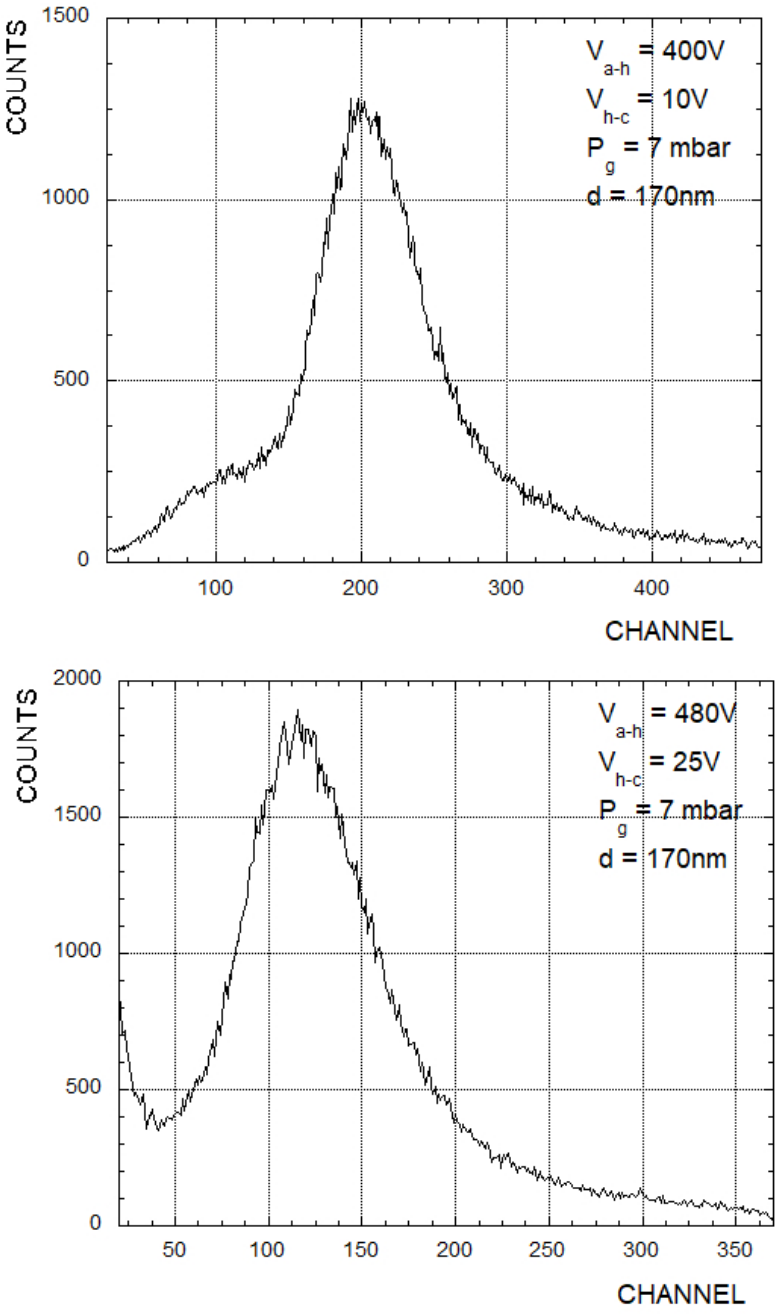

Figure 3.3: MiMi energy spectra obtained with the exploitation of the internal ^{244}Cm alpha source.

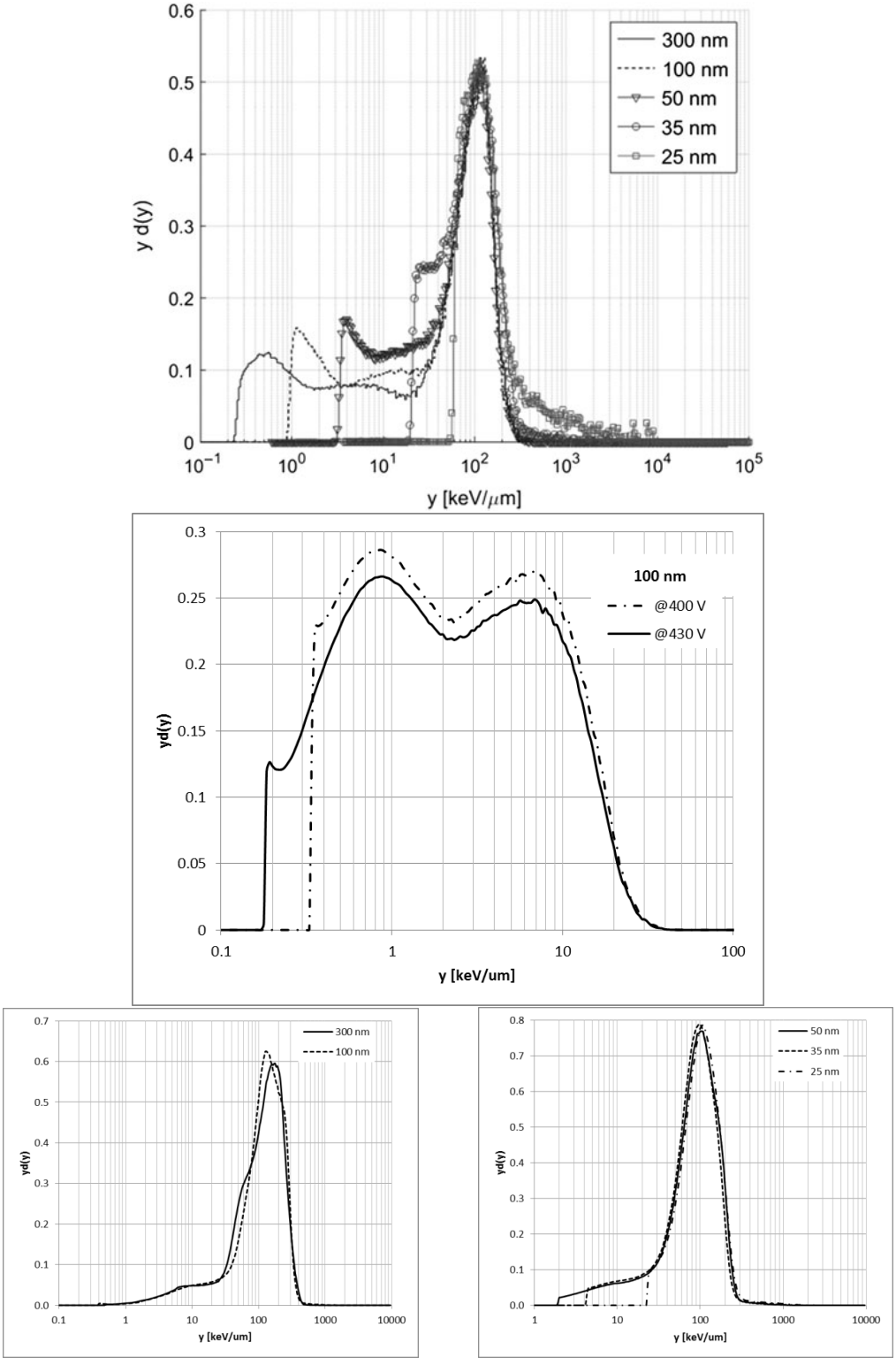

Figure 3.4: Top: Neutron microdosimetric spectra at 300, 100, 50, 35 and 25 nm in site size measured by irradiating the TEPC with 0.64 MeV neutrons [38]. Middle: Dose distributions yd(y) obtained by irradiating MiMi with a Cs-137 gamma source for a simulated site size of 100 nm at different ΔV_{a-h} [37]. Bottom: Microdosimetric spectra obtained by irradiating the MiMi TEPC at the reference depth of 6.76 mm with a 62 A/MeV carbon ion beam at 300 nm and 100 nm (left) and 50 nm, 35 nm and 25 nm (right) [37].

Chapter 4

The Novel MiMi2 TEPC

This chapter is dedicated to the description of the first part of the experimental work of the thesis: the design and the assembly of the novel avalanche-confinement TEPC, named MiMi2.

4.1 Detector Design

The novel detector was designed in order to satisfy some peculiar requests: MiMi2 was projected so that it could properly work down to nanometric simulated site sizes, and be collocated in the same vacuum chamber as the StarTrack counter. In addition, it should be as similar as possible to the MiMi TEPC, in order to make the spectra comparison straightforward.

The first and the last requests defined the component materials and dimensions. Likewise MiMi, MiMi2 has a cylindrical sensitive volume of 13 mm both in diameter and height and consists of three different electrodes independently biased: a central anode wire (graphite, 1 mm in diameter), a cylindrical cathode shell (conductive plastic A-150 type, 13 mm in internal diameter and 1 mm in thickness) and a helix (gold-plated tungsten, 100 μm in diameter).
The helix is made of 19 coils, 6 mm in diameter, and surrounds the anode wire thus subdividing the sensitive volume into the drift and the multiplication regions, which respectively constitute 78.7% and 21.3% of the total volume. Two

field tubes (stainless steel, 6 mm in diameter) are exploited to both sustain the helix and correctly define the sensitive volume, avoiding any distortions of the electric field, while two insulating Rexolite caps enclose the chamber.
The fact that MiMi2 has to be placed in a vacuum chamber makes so that it has not to be sealed: the gas inlet and outlet through the sensitive volume are carried out by acting on the chamber itself. Unlike MiMi, the novel detector is not contained in an aluminium sealed case, but it is protected by a plastic one that lets the gas pass through an apposite slot.
The slot is not only carved in the plastic protection, but in the cylindrical plastic cathode too in order to make particles and beams enter the sensitive volume without losing too much energy or even stopping within the plastic components. In this way, MiMi2 can work together with the StarTrack counter: the same particle beam is able to cross the microdosimeter sensitive volume before reaching the StarTrack counter, thus depositing signal in both detectors and making it possible to correlate the two of them.
A further consideration has to be done about the materials that compose the detector. In particular, the plastic (Shonka A-150 type) constituting the cathode shell is the reference material exploited for the construction of microdosimeters as it manages to satisfy some minimal requests. The first is to be a good conductor, as it has to constitute one of the electrodes of our TEPC. The second is to have a chemical composition as close as possible to both that of the standard tissue defined by the International Commission on Radiation Units and Measurements (ICRU) so that it can adequately satisfy the simulation principle, and to the gases that are going to fill in, in order to fulfill the Fano's theorem (see Table 3.1). The Shonka plastic was developed in 1958 by Francis Shonka as a mixture of calcium fluoride, polyethylene, nylon and carbon so that it also resulted strong, machinable, moldable, chemically stable and had a low gas permeability.
Figure 4.1 show a sketch of MiMi2 cross sectional view.

The components shapes and dimensions of the novel detector have been evaluated by exploiting a dedicated code [39].
In a non relativistic situation, the basic Monte Carlo treatment of the motion of charged particles submitted to an electric field is stochastically described by the

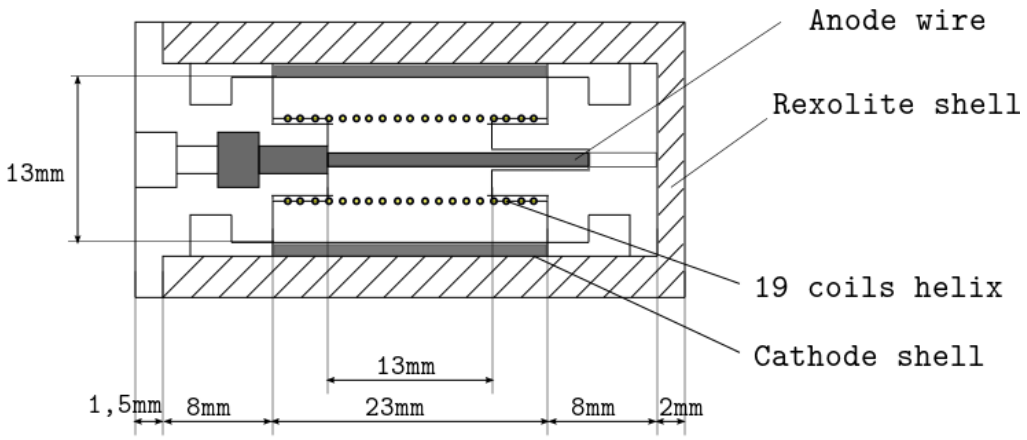

Figure 4.1: Sketch of MiMi2 cross sectional view. See text for details.

probability laws of scattering and the Newton equations. The main quantity to be determined in order to develop the calculations is the time of flight τ between two collisions, and it can be generally obtained by solving the equation

$$\tau = \frac{1}{v_\tau} ln\left(\frac{1}{1-R}\right) \tag{4.1}$$

where

$$R = \int_0^\tau exp\left(-\int_0^u v_\tau\big(\epsilon(\zeta)\big)\, d\zeta\right) du \tag{4.2}$$

is a random number distributed between 0 and 1, ν_τ is the total collision frequency which depends on the electron energy ϵ, which is a function of time.

From the knowledge of the time of flight, the location and the energy of the particles can be obtained from the Newton equations, which can be written in a cylindrical geometry as

$$\begin{aligned} \frac{dz}{dt} &= v_z & \frac{d\,v_z}{dt} &= \gamma_z \\ \frac{dr}{dt} &= v_r & \frac{d\,v_r}{dt} &= \frac{v_\theta^2}{r} + \gamma_r \\ \frac{d\theta}{dt} &= \frac{v_\theta}{r} & \frac{d\,v_\theta}{dt} &= -\frac{v_r\, v_\theta}{r} \end{aligned} \tag{4.3}$$

where γ_z and γ_r are the longitudinal and radial acceleration of the particle, v_z, v_r and v_θ are respectively the longitudinal, radial and transversal velocities.

In a non uniform electric field, as it is our situation, the Newton equations can not be exactly integrated, and a numerical integration by using a standard solver

for the first order differential equations is required. This numerical approach aims at calculating the physical quantities of interest by reconstructing the primary and secondary electron paths inside the detector.

The previously described code has to be developed in order to properly describe the presence of a third electrode represented by the helix, that confines the avalanche from the drift region. In particular, the Monte Carlo treatment of the transport of the electrons in the helix counter is difficult as the electric field generated no more possesses a cylindrical symmetry. This implies some restrictions on the boundary assumptions that were made to develop the code: in particular, the Monte Carlo calculations assume a counter of infinite length, which means that the motion of electrons is only considered in a small part of the detector, the length of which being equal to a helix period. When the electron leaves this region it is immediately injected on the opposite side in order to assure the continuity of motion, as the electric field components undergo a continuous variation from plane to plane along the z axis.

As an example of the numerical results obtained from the code, Figure 4.2 shows a comparison between the radial components of the electric fields for an ideal cylindrical counter and a helix counter of the same dimensions.

4.1.1 The Helix

The MiMi2 TEPC was designed in order to measure microdosimetric spectra in simulated sizes from 300 down to 25 nm. When dealing with small gas pressures the electronic avalanche tends to occupy all the detector volume. When this happens, the multiplication factor depends on the first interaction position and the energy resolution results irreparably spoiled. As we already mentioned, a possible solution to overcome this problem is the confinement of the avalanche region in a small central volume by introducing a third electrode between the cathode and the anode wire: the helix.

If this third electrode is properly biased, electrons generated in the drift zone move towards the helix without inducing other ionization processes and undergo the same multiplication process regardless the actual position at which they are generated. Nevertheless, the helix could absorb some of the electrons drifting towards the anode, thus leading to a decrease of the detector gain [40].

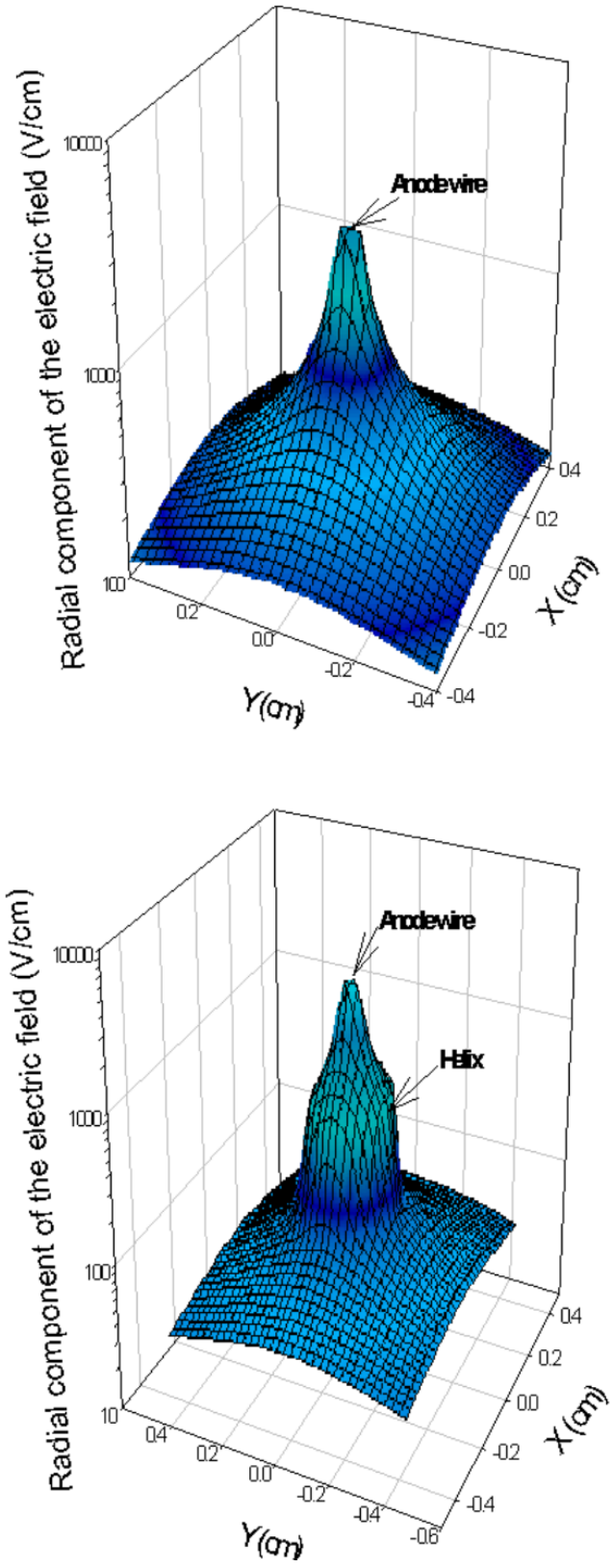

Figure 4.2: Radial component of the electric field for a pure cylindrical geometry (top) and for an infinite helix counter (bottom).

As previously showed, the presence of the helix radically changes the electric field behaviour inside the detector. As we already mentioned, in a cylindrical geometry the electric field along the radial distance r is described by the following relation:

$$E(r) = \frac{V_a - V_c}{r\, ln\left(\frac{r_c}{r_a}\right)} = \frac{K}{r} \tag{4.4}$$

where V_a and V_c are the applied voltage to the anode and cathode respectively, r_a and r_c are the radii of the anode wire and the cathode, $K = \frac{V_a - V_c}{ln\left(\frac{r_c}{r_a}\right)}$ is a factor which depends only on the size of the counter and the applied voltages.
The presence of the helix essentially induces the separation of the inner volume into two coaxial counters.
The inner one is delimited by the anode and the helix, which behaves cathode-like. This is the multiplication region. Its behaviour is determined by the voltage difference ΔV_{a-h}, and more specifically by the electric field towards the anode E_a:

$$E_a(r) = \frac{V_a - V_h}{r\, ln\left(\frac{r_h}{r_a}\right)} = \frac{K_{in}}{r} \tag{4.5}$$

The external one is delimited by the cathode and the helix, which behaves anode-like. This is the drift region. Its behaviour is determined by the voltage difference ΔV_{h-c}, and more specifically by the electric field towards the cathode E_c:

$$E_c(r) = \frac{V_h - V_c}{r\, ln\left(\frac{r_c}{r_h}\right)} = \frac{K_{out}}{r} \tag{4.6}$$

where V_a , V_h and V_c are the applied voltages to the anode, helix and cathode, respectively; r_a , r_h and r_c are the radii of the anode wire, the helix and the cathode, respectively; K_{in} and K_{out} are the electric field shape factors inside and outside the helix, respectively.

4.2 Detector Assembly

The Mimi2 TEPC has been designed in order to be assembled as much as possible by only interlocking the different components. This aims to make it simpler to disassemble it in case of repair.

The primary involved components are:

- the cylindrical cathode shell divided in two halves along its height, made of Shonka plastic A-150 type: 13 mm in diameter, 39 mm long and 1 mm thick;
- the central anode, made of nuclear graphite: a 36.5 mm long and 1 mm thick cylinder in the sensitive part, 1.5 mm and 2.5 mm thick in its joint parts;
- the helix, made of Au-W plated: 19 coils, 13 mm long and 6 mm in diameter;
- the internal core, made of Rexolite 1422: a two carved pieces cylindrically symmetrical and isolating support, for a total 60 mm length, capable of containing the graphite anode and maintaining the cathode shell halves, as well as isolating the central anode from the external shell;
- a M3-M2 brass screw, exploited to stop the anode graphite from the first to the second piece of the internal core;
- a cylindrical Rexolite 1422 external shell, with slots carved on both its bases in order to let the particle beam pass, acting as a container for the whole detector;
- two stainless steel field tubes, 6 mm in diameter, exploited to both sustain the helix and correctly define the sensitive volume, whose edges have been properly smoothed in order to avoid any distortions of the electric field.

Figure 4.3 shows some pictures of MiMi2 components during the detector assembly.

As already mentioned, most of the components of Mimi2 have been assembled by interlocking them. Exception is done for the helix: the 19 coils grid has been glued together with its connector onto the Rexolite internal support with the Master Bond EP21TDCS, a two component, silver filled, electrically conductive adhesive glue.
Different holes were drilled in the cylindrical Rexolite shell in order to take inside the bias high voltage for the electrodes and to take out the connectors for the signals of the helix and the cathode. On the other hand, the anode connector is represented by the brass screw itself.
Figure 4.4 shows the completed MiMi2 detector inside its support.

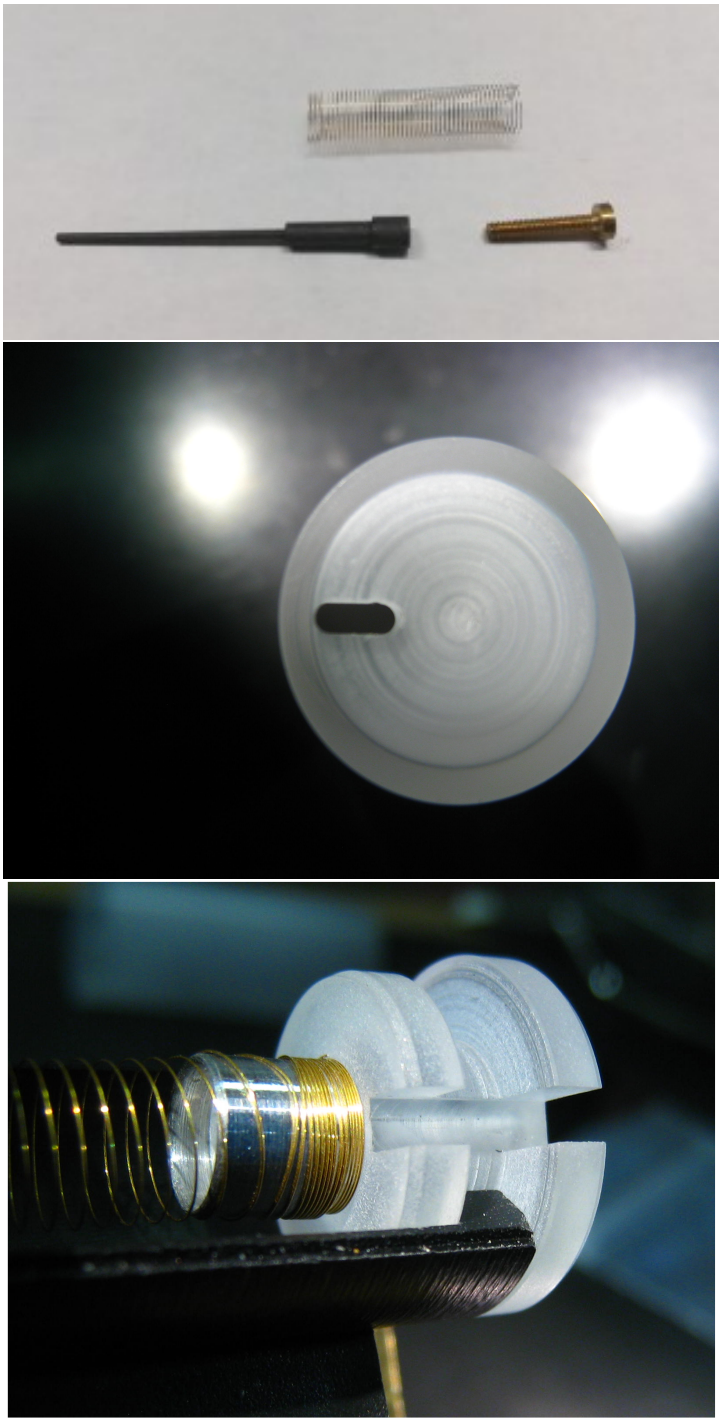

Figure 4.3: Details of Mimi2 components.
(Top) The Au-W plated helix, the graphite anode and the brass screw.
(Middle) The back of the cylindrical Rexolite external shell with the carved slotO.
(Bottom) Half of the cathode shell and the helix sustained by the field tube onto the internal Rexolite support. See text for details.

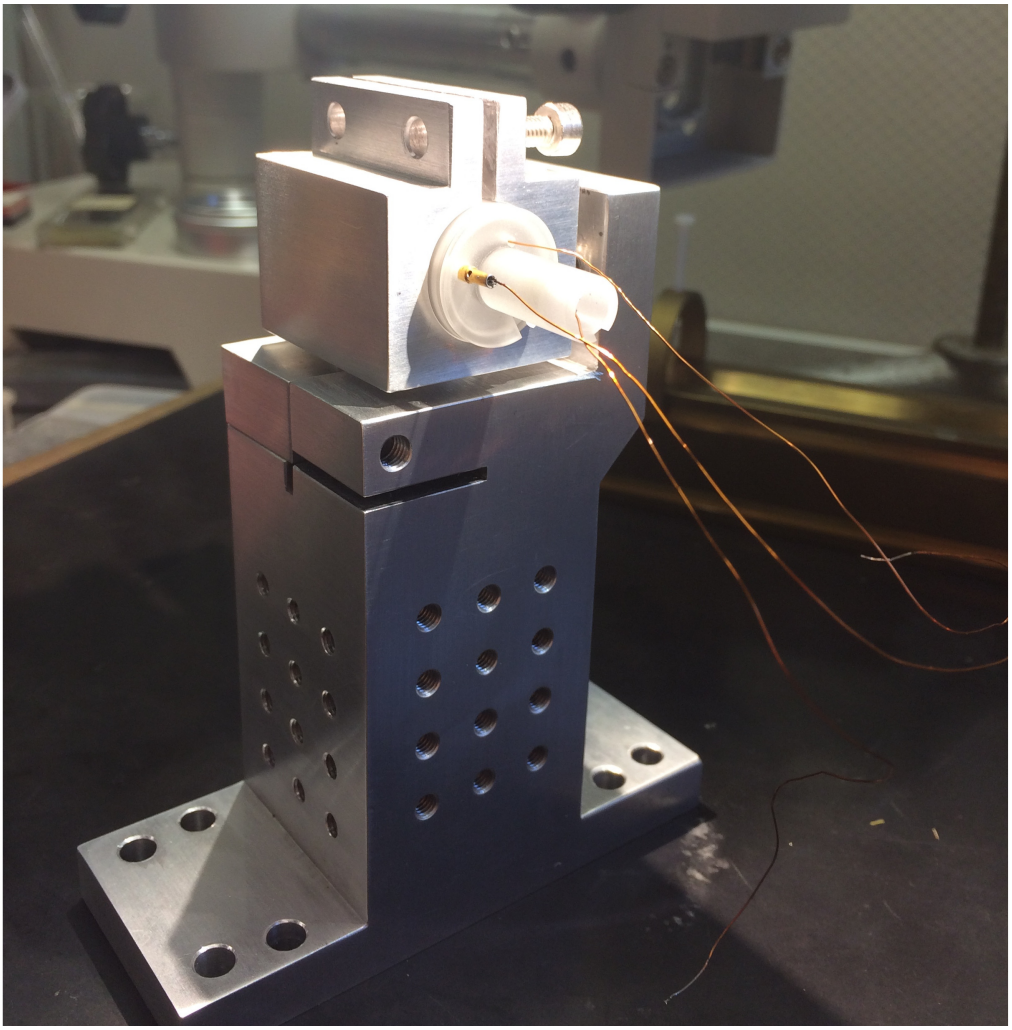

Figure 4.4: The assembled MiMi2 detector inside its support. One can clearly see the anode, helix and cathode electrode cables coming out of the cylinder. See text for details.

Since the detector has to work at low pressures, when dealing with high voltages and signal transport, one has to take into account the necessity of exploiting determinate materials and to take care of particular details in order to avoid electrical discharges.

In particular, in addition to the presence of close electrical components tips, the breakdown voltage between two electrodes, i.e. the voltage necessary to start a discharge or electric arc, depends on the gas type and pressure, on the gap length between the electrical components and on the acting electric field. The Paschen's law [41] is an empirical formula that defines the breakdown voltage as a function of gas type and pressure P, and gap length between the considered electrodes. Nevertheless, for a given gas the formula simplifies, and the breakdown voltage

depends only on the product of the pressure and gap length, or equivalently on the reduced electric field, defined as:

$$E_p = \frac{E}{P} \tag{4.7}$$

where E is the electric field and P is the gas pressure.
Once evaluated the gas type and pressure of work and the bias voltage involved, in order to avoid electrical discharges one has to consider both some minima gaps between the various electrical components and the application of special isolating glues and thermofit cable covers.

4.2.1 Detector Installation

As it will be further described in section 5.1.1, the vacuum chamber containing the StarTrack apparatus is divided into two different volumes. That of our interest, in which the Mimi2 detector and its ancillary devices have been installed, is a 280 mm · 130 mm base parallelepiped.
A sketch of the optical perforated plate is reported in Figure 4.5.

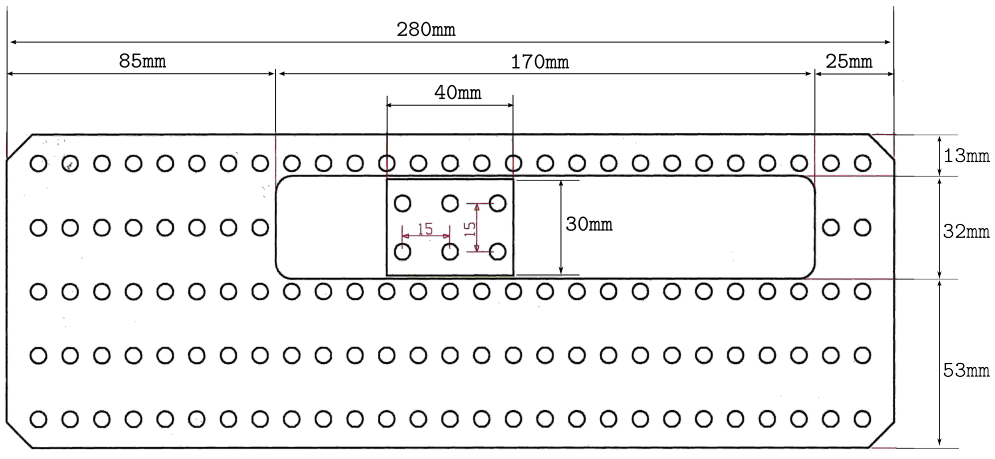

Figure 4.5: Sketch of the optical perforated plate equipped with the moving carriage. See text for details.

The accessory devices consist of:

– an aluminium support that holds the detector at the correct height;

– the alpha source together with its collimating container;

– a second aluminium collimator.

The installation countertop is a perforated optical plate equipped with a moving carriage, whose motors are remotely controlled via a dedicated program. Although the final configuration will provide for the collocation of MiMi2 on the moving carriage, in order to execute the first functional tests the detector has been secured on the unmovable part of the perforated plate, while the alpha source and the collimator have been fixed on the moving carriage. This different collocation of the involved devices has been due to some technical issues: in particular, this provisional configuration is owed to the fact that, while the ultimate miniaturized preamplifier board will be mounted on the detector support itself, the temporary preamplifier was too big to fit on the moving carriage together with MiMi2.
Although the functional test measurements do not require beam particles but a removable calibration alpha source, the described elements have been installed in order to result in a correct line-up with the beam line, so that an adequate alignment procedure could be executed between the detector and the alpha source by exploiting the fixed laser pointer that equips the StarTrack apparatus.
Figure 4.6 shows a picture of the fully equipped StarTrack apparatus, while Figure 4.7 and 4.8 present Mimi2 together with its support, the alpha source and the collimator, inside the opened StarTrack vacuum chamber.

The installation of the previously described devices has been performed by paying particular attention to some features. Specifically, all the connections passing through the flanges of the vacuum chamber have been isolated through Rexolite tubes, in turn sealed with Torr Seal, which is a two parts low vapor pressure epoxy resin. This ensures good electrical isolation and leakproofness of the connectors.
In addition, all high-voltage cables are kapton covered. Kapton is a polyimide film particularly indicated for our scope as it both ensures an optimum electrical isolation and a low outgassing rate, which is an essential feature when dealing with high vacuum and operating with gases whose pureness is crucial for the measurements.
Finally, the weld joints of both the high- and the low-voltage cables have been

electrically isolated by exploiting non-conducting glue and thermofit heat shrinking tubing.

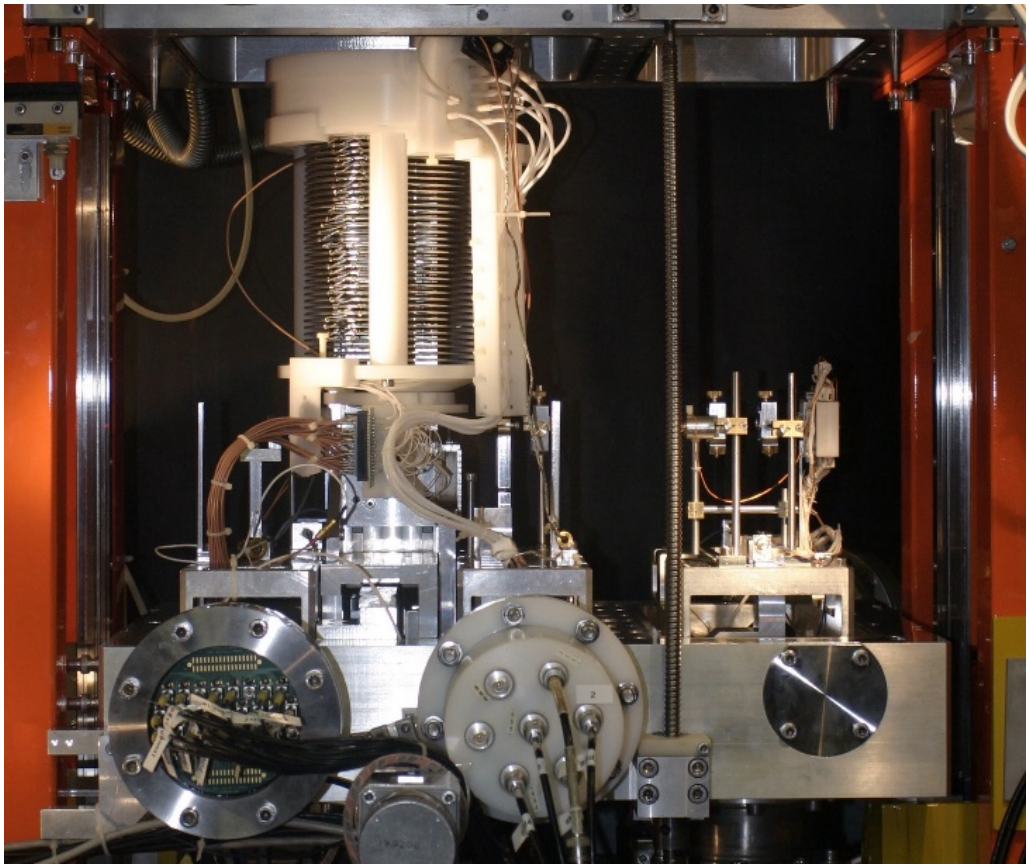

Figure 4.6: Picture of the StarTrack vacuum chamber. See text for details.

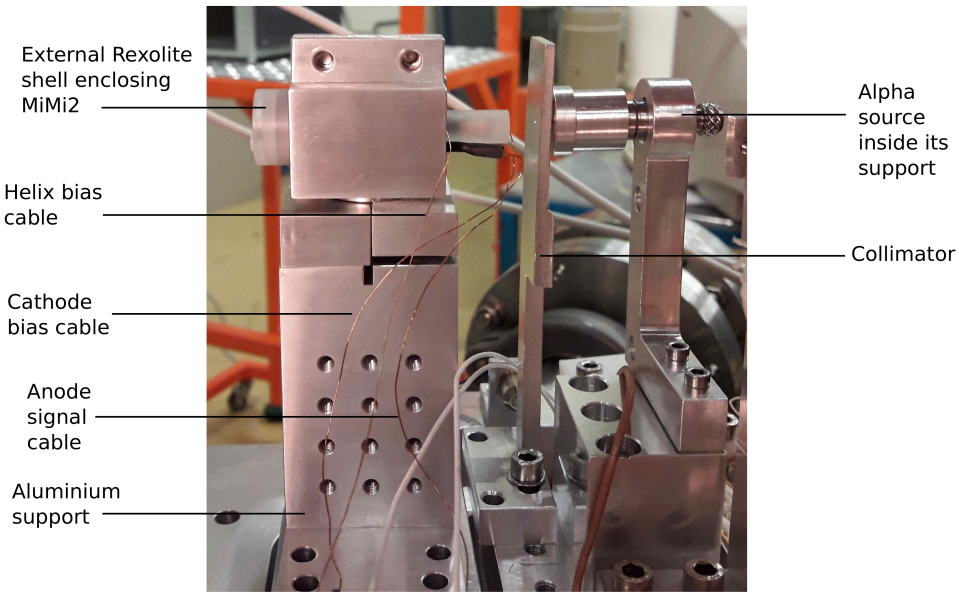

Figure 4.7: MiMi2 together with its support, bias and signal cables (left), the alpha source and the collimator (right). See text for details.

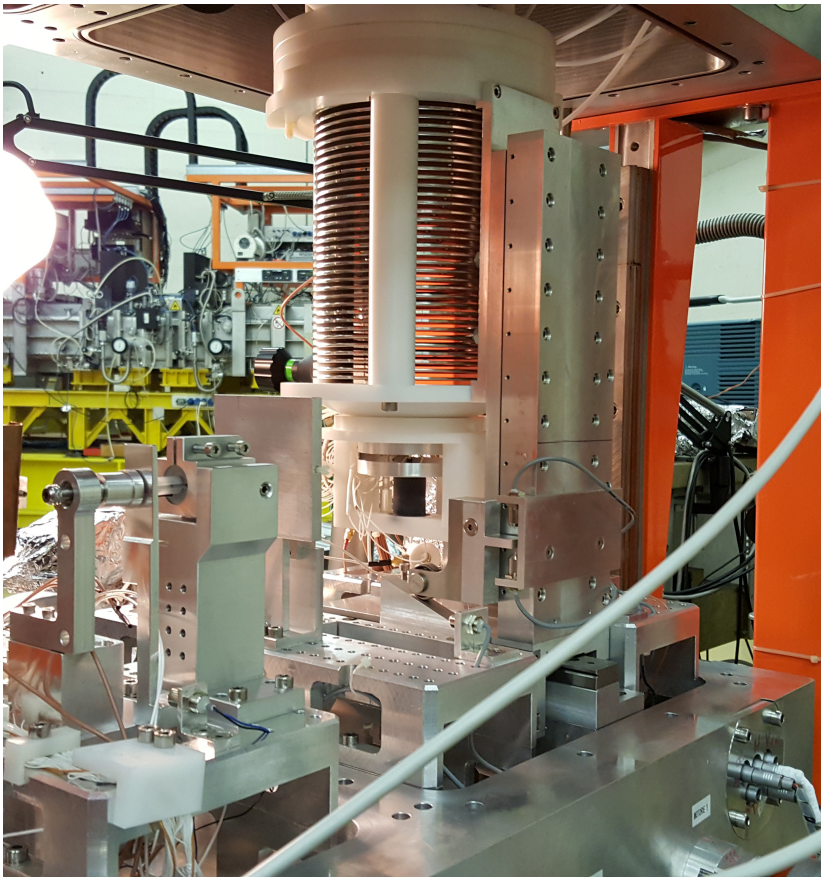

Figure 4.8: MiMi2 and its ancillary devices (left) inside the opened vacuum chamber on the background of the StarTrack drift column. See text for details.

Chapter 5

Data Collection, Analysis and Results

This chapter is dedicated to the description of the second part of the work of thesis: the first functional tests of the novel avalanche-confinement TEPC, MiMi2.

5.1 Experimental Set-Up

As already mentioned, MiMi2 was designed in order to provide microdosimetric spectra in coincidence with the nanodosimetric ones of the Startrack apparatus in Legnaro.
In order to execute the first functional tests, the detector was placed inside the pre-chamber of the StarTrack apparatus, thus requiring some particular expedients and re-arrangements in the gas flow system and the electronic set-up.

5.1.1 Vacuum and Gas Flow System

The StarTrack vacuum chamber apparatus (see Figure 5.1) is composed of:

– two vacuum chambers separated via a mylar window, that allows the beam to pass from the first (pre-chamber) to the second volume (allocation for the StarTrack drift column counter);

– a turbomolecular pump (Pfeiffer/Balzer TMU 262P) acting on the pre-chamber;
– a second turbomolecular pum (Alcatel PTM 5150) operating on the chamber;
– two frictionless multi-stage roots pumps (Alcatel Adixen ACP 15), one exploited as a pre-vacuum pump for the whole system, the other as a pre-atmospheric pump for the turbomecular pump operating on the chamber;
– a dry scroll pump (Varian SH-100) that acts as a pre-atmospheric pump for the turbomolecular Pfeiffer/Balzer TMU 262P;
– a second dry scroll pump (Varian SH-110) operating as a pre-atmospheric pump for the outlet gas line;
– a turbomolecular pump exploited for the outlet gas line;
– Pirani gauges;
– manual and electro- valves.

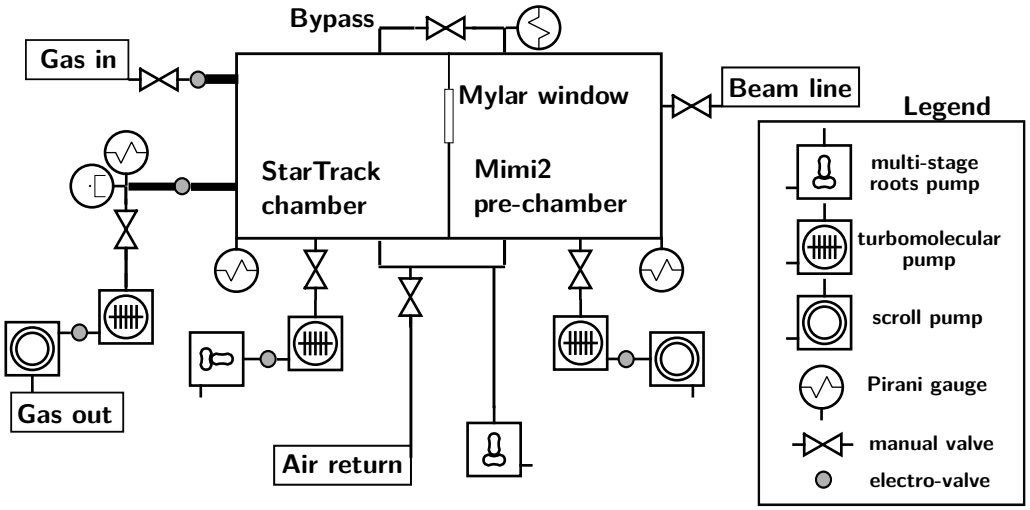

Figure 5.1: Schematic diagram of the StarTrack vacuum chamber and gas flow system that have been exploited for the MiMi2 test measurements. See text for details.

Originally, the apparatus was made so that gas inlet an outlet were only possible for the Startrakc chamber. The pre-chamber, designed for beam diagnosis and collimation in vacuum, has been exploited for our purpose: the installation of Mimi2 in the pre-chamber required the gas flow to go through this volume too. In order to do that, a bypass has been properly assembled.

As one can see from Figure 5.1, each of the two chambers is equipped with a

rotative and a turbomolecular pump, separated each other via an electrovalve controlled via a Pfeiffer Vacuum DualGauge system. A pre-vacuum scroll pump depletes the inner volume from atmospheric pressure to $\sim 10^{-2} - 10^{-3}$ mbar for both chambers. The two turbomolecular pumps are independent, and are electronically enabled only when the low-vacuum pressure reaches a setted value. In order to monitor the vacuum and gas pressure, each chamber is provided with a Pirani and a Penning vacuum gauges.

The gas flow system is independently integrated in the apparatus. It comprehends a gas tank, an MKS PR-3000 gas flow controller and its own Pirani and Penning vacuum gauges collocated on the outlet line, which is made of a scroll and a turbomolecular pump. When the two chambers reach a sufficiently high vacuum, which for our measurement purpose is about 10^{-6} mbar, the valves communicating with the vacuum pumps are closed, leaving only the gas outlet line ones enabled. The gas inlet from the tank is regulated via the MKS flow controller, which sets the proper opening for the related valve. In order to maintain a constant pressure, a feedback system regulates the opening of the gas outlet line valve. A continuous gas flow permits both the maintenance of the desired pressure, which represents a precise simulated site size, and the replacement of the DME we used for our measurements, in order to avoid the gas deterioration as far as possible.

5.1.2 Electronic Chain, Signal Processing and Acquisition System

The electronic chain and the data acquisition system (see Figure 5.2) are composed of:

- $\pm$12 Dual Power Supply (mod. EX354RD);
- a dedicated charge-sensitive preamplifier;
- a Precision Pulse Generator PB-4;
- a Tektronix DPO 4032 Digital Phosphor Oscilloscope;
- a Spectroscopy Amplifier and Gated Integrator (Ortec mod.673);
- a 14 bit ADC (16K, module AD114);
- a Quad Bias Supply (Ortec mod. 710).

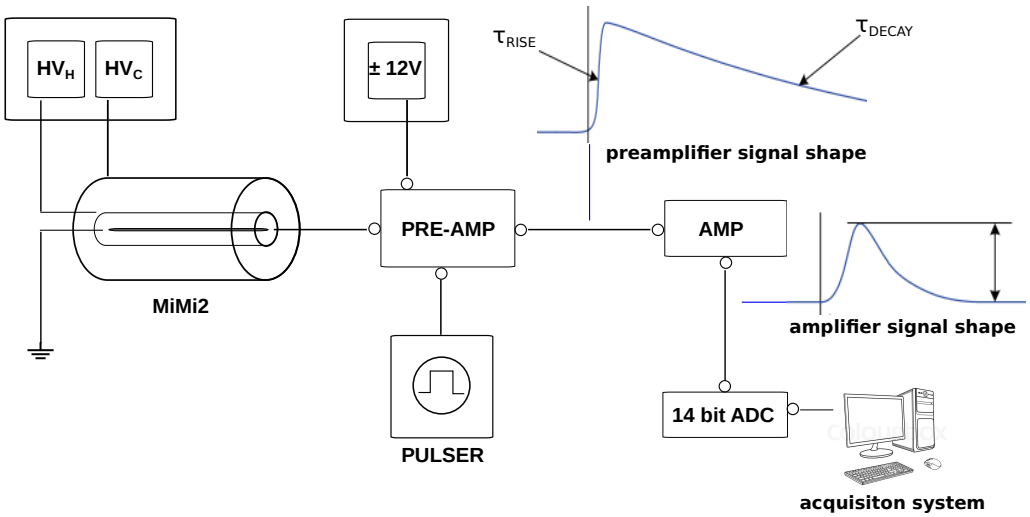

Figure 5.2: Sketch of the electronic chain and data acquisition system. See text for details.

Both the cathode wall and the helix are biased via a Quad Bias Supply, which provides high continuous negative voltage, while the anode wire is earthed. Proper isolated connections have been placed through the vacuum chamber flange in order to keep a stable high voltage and to minimize disruptive discharge events. Once a charged particle crosses the sensitive volume of MiMi2, which is an α particle in the case of our test measurements, electrons drift towards the helix and undergo a multiplication process in the avalanche region. The resulting electrons are collected from the anode wire, whose output is sent to a dedicated preamplifier that is enclosed in the vacuum chamber in order to reduce as far as possible the electrical noise introduced by cables, thus maximising the SNR ratio. This module provides both a preliminary amplification of a factor $\times 10$ and a preliminary shaping of the signal: the rise time is related to the charge collection time and amounts to a few tens of nanoseconds, while the fall time depends on the RC of the preamplifier, and consists of $\sim 10^2$ ms. The preamplifier is biased via a Dual Power Supply which provides a ± 12 bias voltage.

Then, the signal is sent to a Spectroscopy Amplifier and Gated Integrator, which both models the signal into a gaussian shape and applies an amplification factor once imposed proper shaping time and gain.

In order to set the proper parameters in the electronic chain modules, a square test signal is provided by a Pulse Generator module, which simulates the arrival of a voltage pulse from the detector via a dedicated connection placed onto the

preamplifier board.
The resulting potential difference signal is finally collected in a peak-detector 14 bit 16K ADC module AD114, which linearly associates the gaussian peak amplitude to one of the available channels.
The final spectra are collected by the dedicated K-Max acquisition program, which allows a threshold setting in order to optimize the dead time.

5.2 The Electron Transmission Windows

A first experimental investigation was performed in order to find the best working conditions of MiMi2 by exploiting a ^{244}Cm alpha source.
At each different gas pressure P (i.e. for each simulated site size d), the fundamental parameters to be optimized are the bias voltages of the cathode and the helix, while the anode wire has been earthed throughout all the measurements.
Once the gas pressure was selected, the choice of the voltage difference ΔV_{a-h} between the anode wire and the helix was made in order to ensure the highest gain without any electronic discharge.
At each value of pressure P and voltage difference ΔV_{a-h}, the characterization of the detector response has been performed in terms of amplitude of the TEPC signals generated by alpha particles as a function of the cathode bias voltage V_c, or equivalently as a function of the voltage difference ΔV_{h-c} between the helix and the cathode.
The purpose was to evaluate a proper ΔV_{h-c} value which:

- ensures the confinement of the electronic avalanche inside the multiplication region, delimited by the helix;
- prevents the recombination of ions and electrons in the drift region between the helix and the cathode;
- minimizes the absorption of electrons by the helix, to prevent unwanted counter efficiency reduction.

The first two points require a voltage difference between helix and cathode ΔV_{h-c} low enough to prevent any multiplication event inside this region, but at the same

time high enough to prevent the ion-electron recombination.

Various random factors intervene in determining the shape of the pulse height distribution observed when a proportional counter is traversed by charged particles, concerning both the distribution of energy absorbed in the gas and the modification of this distribution by the measuring system.
Neglecting additional factors that are frequently unimportant in small sites (such as change of LET during traversal or finite particle range), they are:

- The distribution of the number of (energy deposition) events;
- The LET distribution of the particles;
- The distribution of the path lengths of particles in the site;

that collective properties of all particles. Other causes of fluctuations, involving energy deposition by individual particles, are:

- The distribution of the number of collisions;
- The distribution of energy imparted in individual collisions;
- The distribution of the fraction of this energy retained in the site (i.e. not escaping as delta radiation).

The distribution of the total charge collected when an event produces n ions in the counter is the n-fold convolution of the single electron spectrum when there is no mutual interference between avalanches. The spectrum for single electrons can be well approximated by a Polya distribution:

$$p_1(x) = a \cdot x^b e^{(-c \cdot x)} \tag{5.1}$$

where b and c are characteristic factors of the exploited gas.

When charged particles deposit equal energy in a proportional counter a range of pulse heights is observed because of the convolution of the various phenomena considered, conferring an approximated gaussian shape to the pulse height distribution. Thus, the TEPC signal amplitude has been evaluated by calculating the centroid of the spectra (see Figure 5.3).

As already mentioned, the amplification gain of the shaping amplifier dedicated to the TEPC signal is not constant, but it changes on the basis of the

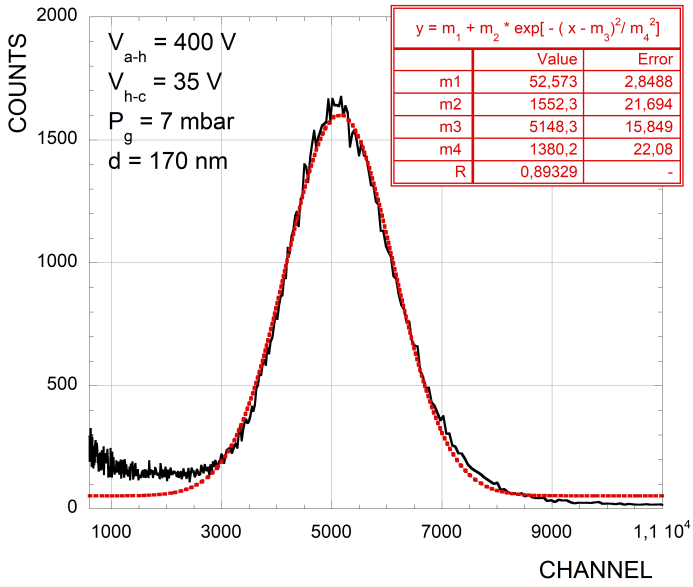

Figure 5.3: Example of gaussian fit performed in order to obtain the TEPC signal amplitude with the corresponding error. Displayed parameters correspond to the gaussian fit formula: $y(x) = m_1 + m_2 \cdot e^{-\frac{(x-m_3)^2}{m_4^2}}$.

simulated site size and on the applied voltages to the electrodes. In order to allow a direct comparison between the measured electron transmission windows, it is necessary to normalize the results through a calibration procedure. This was done for all the different configurations by exploiting a BNC PB-4 Precision Pulser to generate different test square signals at the test input. In such a way, the TEPC signal amplitude, evaluated in mV, is the following:

$$TEPC\,out[mV] = m\left[\frac{mV}{ch}\right] \cdot TEPC\,out[ch] + q[mV] \tag{5.2}$$

where m and q are the slope and the intercept of the calibration curve, respectively.

5.2.1 Simulated Site Sizes and Voltage Differences

The determination of the electron transmission windows involved four different pressures in DME gas, 10 mbar , 7 mbar , 2 mbar and 1.5 mbar, representing the four simulated sizes 240 nm , 170 nm , 50 nm and 35 nm respectively.

The DME gas ($(CH_3)_2O$) exploited for these measurements was 1 cc/min flushed in order not to significantly degrade the gas during data collection.

For each of these four sizes, different ΔV_{a-h} (voltage differences in the avalanche

region) were tested, the optimum ones being listed in Table 5.1. Generally, the maximum value of ΔV_{a-h} is determined by the beginning of electronic discharge. As far as the TEPC under study is concerned, for site sizes which show a high gas gain (170 nm and 240 nm) this limit is given by the saturation of the preamplifier. In this case, a lower ΔV_{a-h} is adequate, since the gain is high enough to produce a proper microdosimetric spectrum. On the other hand, for site sizes which show a low gas gain (50 nm and 35 nm), the upper limit in the ΔV_{a-h} is given by the distortion of the acquired signal, which comes before possibly caused by a charge generation outside the multiplication region.

Gas pressure [mbar]	Simulated size [nm]	ΔV_{a-h} [V]
10	240	350
7.13	170	400
2.08	50	430
1.47	35	450

Table 5.1: Parameters for the characterization of the electrons transmission windows. For each site size, that is for each gas pressure, the tested voltage differences ΔV_{a-h} between the anode wire and the helix are reported.

5.2.2 Results

For each of the simulated site sizes listed in Table 5.1, eight to twelve different ΔV_{h-c} were tested in order to determine the electron transmission windows. Some of them, after a proper rebinning procedure, are shown in Figure 5.4 and 5.5.

Figure 5.6 shows the variation of the TEPC signal amplitude as a function of the voltage difference between helix and cathode, ΔV_{h-c}. Measurements were obtained with a different ΔV_{a-h} depending on the gas pressure (see Table 5.1) and with different settings in the electronic chain.

As one can see, three main trend regions are clearly distinguishable:

– first region: by increasing ΔV_{h-c}, the signal amplitude increases. This region is characterized by weak electric fields near the cathode wall, where ion recombination is likely to occur and reduces the collected electrons giving rise to the signal;

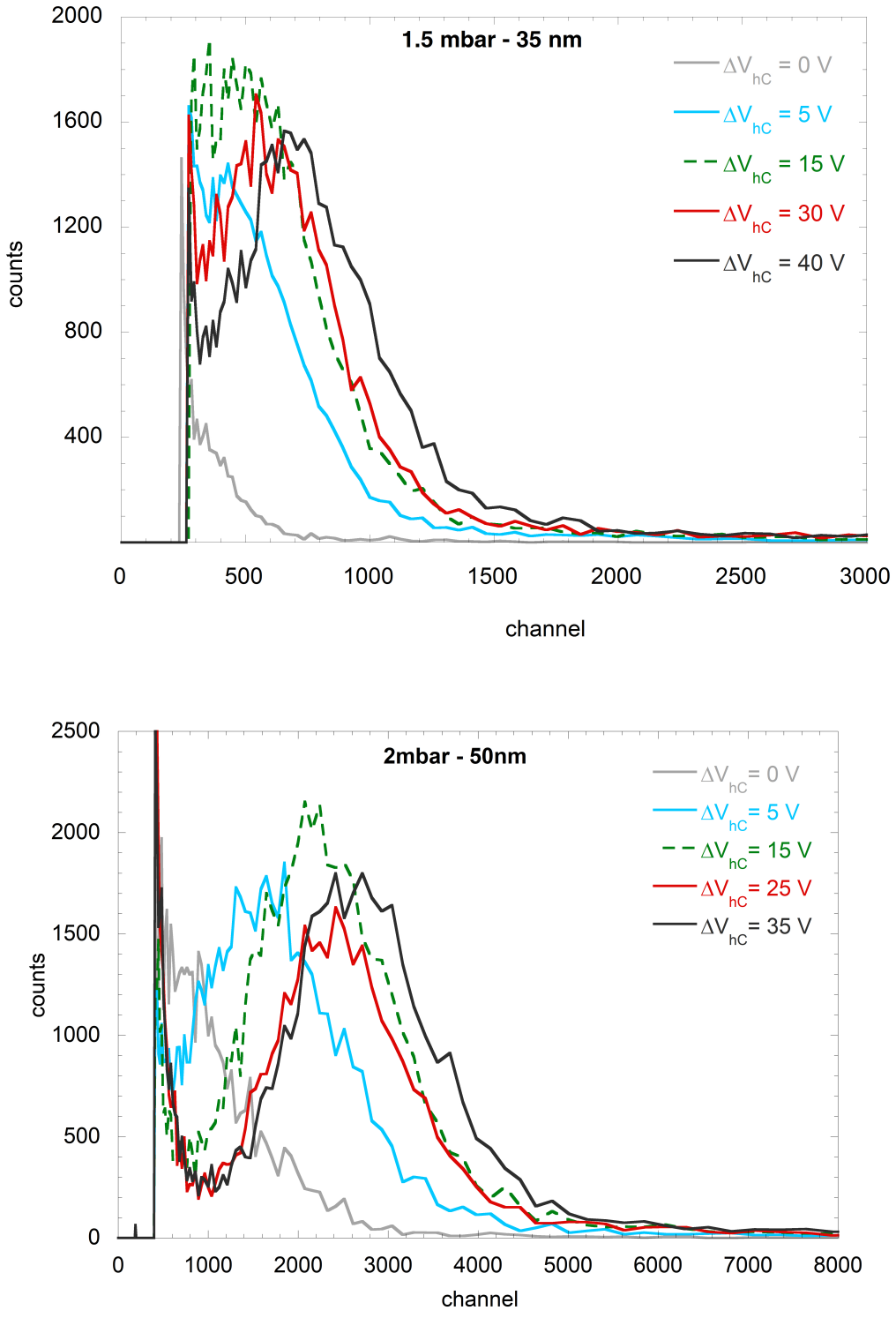

Figure 5.4: Different ΔV_{h-c} non-calibrated alpha spectra exploited for the characterization of the electrons transmission windows: 35 nm simulated site size corresponding to a 1.47 mbar gas pressure with a 450 V ΔV_{a-h} (top), and 50 nm simulated site size corresponding to a 2.08 mbar gas pressure with a 430 V ΔV_{a-h} (bottom). See text for details.

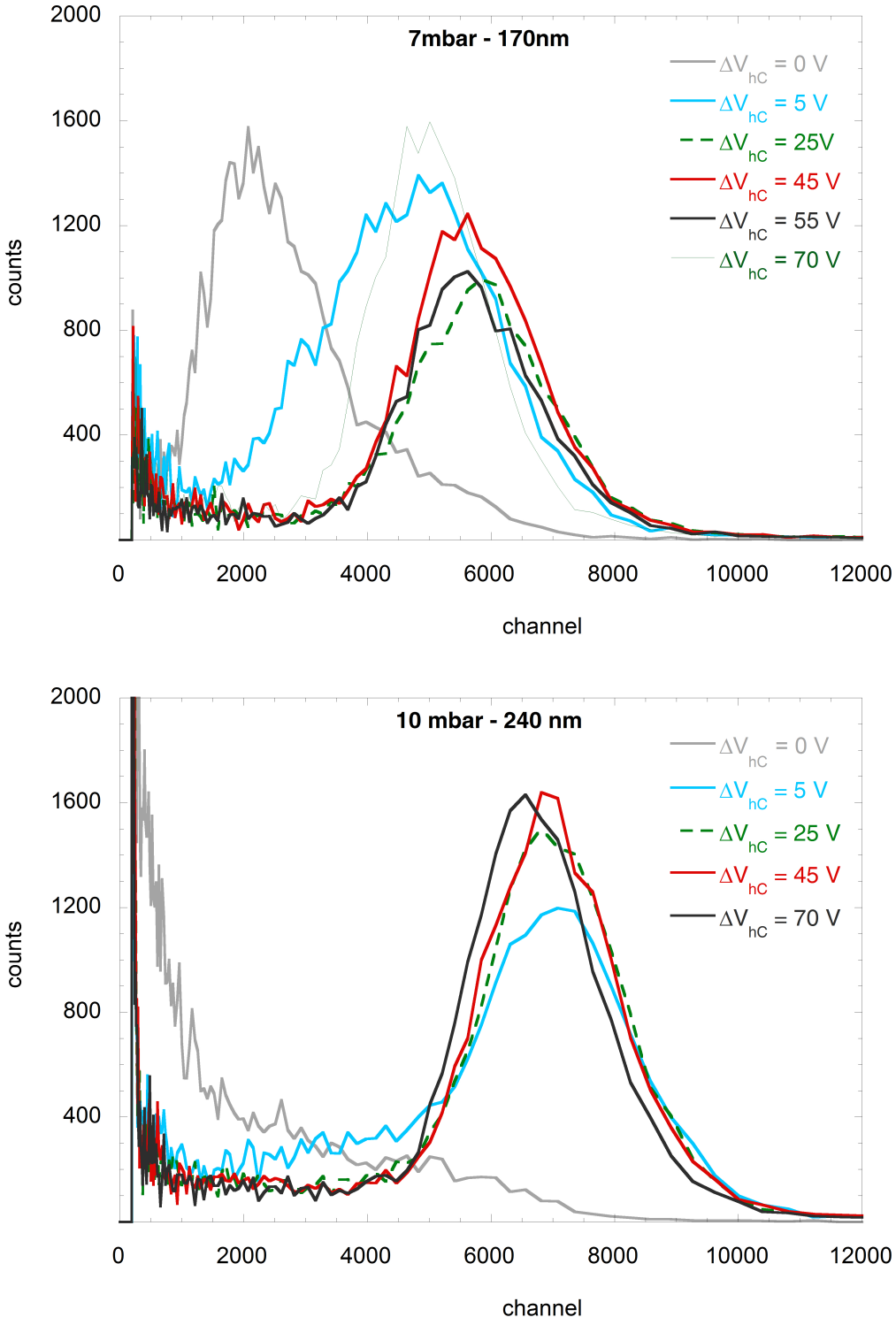

Figure 5.5: Different ΔV_{h-c} non-calibrated alpha spectra exploited for the characterization of the electrons transmission windows: 170 nm simulated site size corresponding to a 7.13 mbar gas pressure with a 400 V ΔV_{a-h} (top), and 240 nm simulated site size corresponding to a 10 mbar gas pressure with a 350 V ΔV_{a-h} (bottom). See text for details.

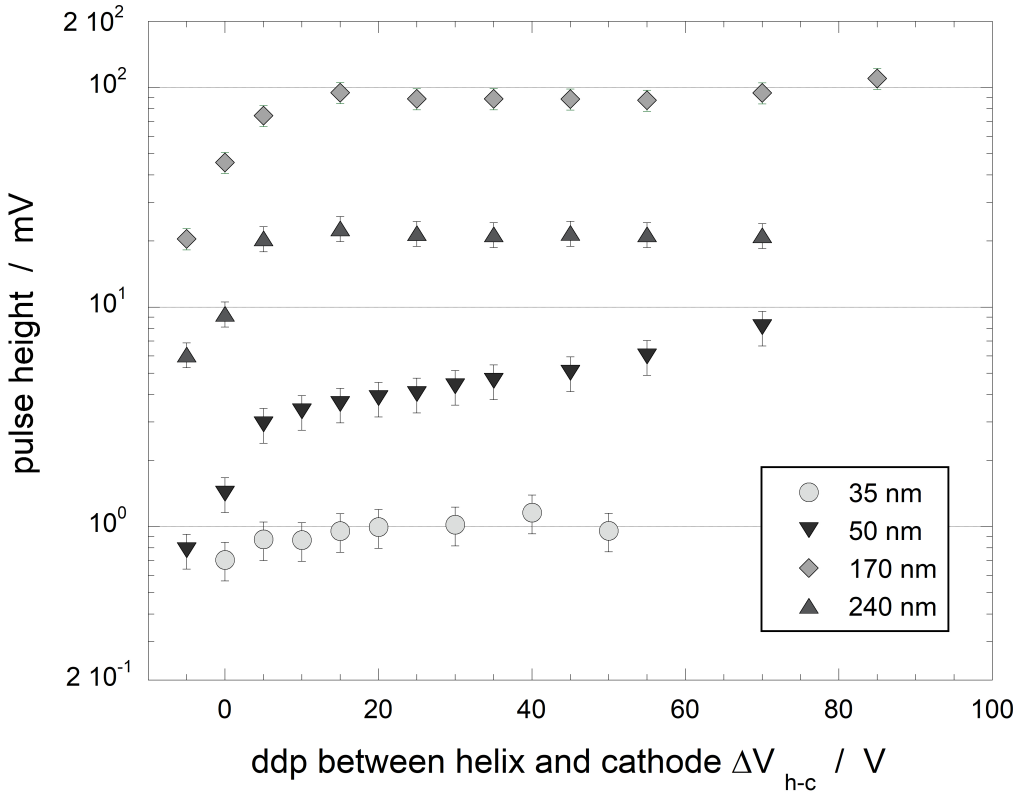

Figure 5.6: TEPC signal amplitudes as a function of the voltage difference between the helix and the cathode of a 35 nm, 50 nm, 170 nm and 240 nm site size. Notice the plot is in a logarithmic scale: signal amplitudes significantly vary with reduced electric field (i.e. gas pressure and ΔV bias). See Table 5.1 and text for details.

- second region: by increasing ΔV_{h-c}, the signal amplitude is constant. In this region it is assumed that no recombination events occur in the drift region, the helix does not absorb electrons and the avalanche is well confined between the helix and the anode wire. This is the so called 'plateau region', in which the response of the TEPC is stable and reproducible. The width of the plateau depends on the gas pressure: at relatively high pressures (corresponding to $d = 170 - 240$ nm) it is generally tens of volts, while at very low pressures it reduces down to a few volts.
- third region: this part is characterized by two coexisting phenomena, whose effects oppose each other in giving rise to the resulting signal amplitudes. These effects are the absorption of electrons by the helix, that leads to a decrease of the signal amplitude, and the 'leakage' of the electronic avalanche outside the helix, which causes higher signals.

As one can see from Figure 5.6, the 35 nm, 170 nm and 240 nm simulated site measurements show a sufficiently large plateau region, where the signal amplitude of MiMi2 remains constant for a ΔV_{h-c} variations range from 15 V to 35 V. On the other hand, the 50 nm simulated site, corresponding to a 2.08 mbar gas pressure, apparently exhibits no plateau region: the signal amplitude increases together with ΔV_{h-c}, though with different slopes. This issue could be due to a bad electric field confinement in the avalanche region at such gas pressure, and requires further investigation for the final characterization of the electron transmission windows.

P_g [mbar]	Site size [nm]	ΔV_{a-h} [V] (ΔV_{h-c} [V])	Signal amplitude [mV] (ϵ_r)
10	240	350 (40)	21.5 ± 2.9 (13%)
7.13	170	400 (35)	90.0 ± 10.2 (11%)
2.08	50	430 (30)	3.9 ± 0.7 (18%)
1.47	35	450 (25)	1.0 ± 0.2 (20%)

Table 5.2: Operating conditions for the novel avalanche-confinement TEPC MiMi2. For each site size, that is for each gas pressure, the voltage differences between the anode wire (a), the helix (h) and the cathode (c) are reported. The setting of the best cathode voltage was performed by selecting a proper value inside the plateau region of the electron transmission windows, following the procedure described in the text.
In addition, for each optimum configuration, the mean values of the signal amplitude has been reported, together with their absolute, expressed as the σ of the quasi-gaussian peak, and relative errors.

5.3 Microdosimetric Spectra

The evaluation of the electron transmission windows determined the best operating conditions for MiMi2, the new avalanche-confinement TEPC.
A second part of the data analysis concerned the calculation of the microdosimetric spectra, which has been implemented by exploiting the same data collection previously described.

5.3.1 Logarithmic Rebinning

Once data have been collected, starting from the channels [ch] of the ADC, the x-axis is converted to voltage amplitudes h [mV] of the test signal through the following relation:

$$h\,[mV] = m\left[\frac{mV}{ch}\right] \cdot ch + q\,[mV] \tag{5.3}$$

where m and q are the slope and the intercept of the calibration curve, respectively, which have been evaluated through test signals provided by the Precision Pulse Generator PB-4 (see Section 5.1.2).
At this point, the pulse height spectrum should be converted to a lineal energy frequency $f(y)$ and dose $d(y)$ descriptions. To do so, a preliminary rebinning procedure is necessary: the linear scale of the acquired raw data has to be converted into a logarithmic binning, typical of the standard microdosimetric representation.
By definition, the normalization of the lineal energy frequency and dose distributions (see Section 2.2.2) requires that:

$$\int_0^\infty f(y)\,dy = 1 = \int_0^\infty d(y)\,dy \tag{5.4}$$

This normalization should remain unchanged when $f(y)$ and $d(y)$ are plotted on a logarithmic scale of y. In such a way, the linear spectrum has to be processed by using the equations:

$$\left.\begin{aligned} d[ln(y)] &= \frac{1}{y} d[y] \\ d[ln(y)] &= d[ln(10) log(y)] = ln(10) d[log(y)] \end{aligned}\right\} \implies d[y] = ln(10)\, y\, d[log\,(y)] \tag{5.5}$$

then resulting in:

$$\begin{aligned} f(y)dy &= y\, f(y)\, d[ln\,(y)] = ln(10)\, yf(y)\, d[log\,(y)] \\ d(y)dy &= y\, d(y)\, d[ln\,(y)] = ln(10)\, yd(y)\, d[log\,(y)] \end{aligned} \tag{5.6}$$

Thus, the normalization of frequency and dose distributions becomes:

$$\begin{aligned} \int_0^\infty f(y)dy &= \int_0^\infty y\, f(y)\, d[ln\, y] = (ln10) \int_0^\infty yf(y)\, d[log\, y] = 1 \\ \int_0^\infty d(y)dy &= \int_0^\infty y\, d(y)\, d[ln\, y] = (ln10) \int_0^\infty yd(y)\, d[log\, y] = 1 \end{aligned} \tag{5.7}$$

The logarithmic scale of y is usually divided into decades, in turns subdivided into N increments per decade, so that the i-th value of y results:

$$y_i = y_0 \cdot 10^{i/N} \tag{5.8}$$

where y_0 is the lowest value of y that has to be considered in the graph.
If the number N of increments per decade is large enough that the difference between $d[log\,(y)]$ and $\Delta[log\,(y)]$ can be neglected, one finds the final relations for the logarithmic normalization for the frequency and dose distributions:

$$\begin{aligned} \int_0^\infty f(y)dy &\approx \frac{ln10}{N} \sum_{i=0}^{\infty} y_i\, f(y_i) = 1 \\ \int_0^\infty d(y)dy &\approx \frac{ln10}{N} \sum_{i=0}^{\infty} y_i\, d(y_i) = 1 \end{aligned} \tag{5.9}$$

Finally, when calculated numerically, these relations result in:

$$\begin{aligned} f(y_i) &= \frac{n_i}{\sum_i n(y_i)\, \Delta y_i} \\ d(y_i) &= \frac{y_i\, n_i}{\sum_i y_i\, n(y_i)\, \Delta y_i} \end{aligned} \quad \Longrightarrow \quad \begin{cases} \displaystyle\int_0^\infty f(y)dy = \sum_{i=0}^{\infty} y_i\, f(y_i)\, \Delta y_i = 1 \\ \displaystyle\int_0^\infty d(y)dy = \sum_{i=0}^{\infty} y_i\, d(y_i)\, \Delta y_i = 1 \end{cases} \tag{5.10}$$

where $\Delta y_i = y_i \cdot (10^{\frac{1}{2N}} - 10^{-\frac{1}{2N}})$ represents the width of the logarithmic interval. As an example, Figures 5.7 and 5.8 show the non-calibrated microdosimetric spectra $h\, d(h) - h$, with h expressed in mV, obtained from the corresponding pulse height raw data.

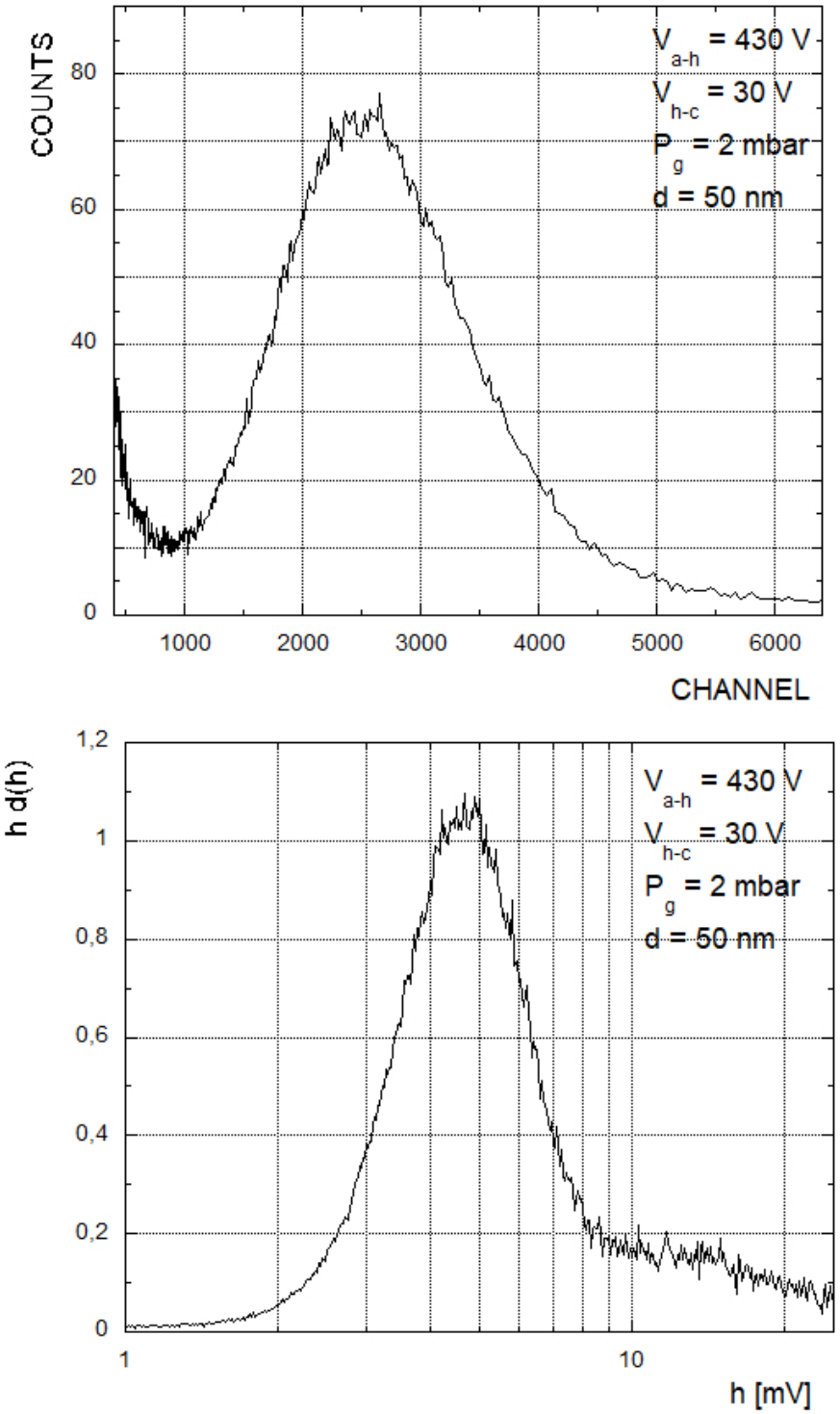

Figure 5.7: (Top) Example of TEPC alpha spectrum obtained with a 2 mbar gas pressures, corresponding to a 50 nm site size, and the corresponding microdosimetric alpha spectrum $h\,d(h) - h$ in mV (bottom). See text for details.

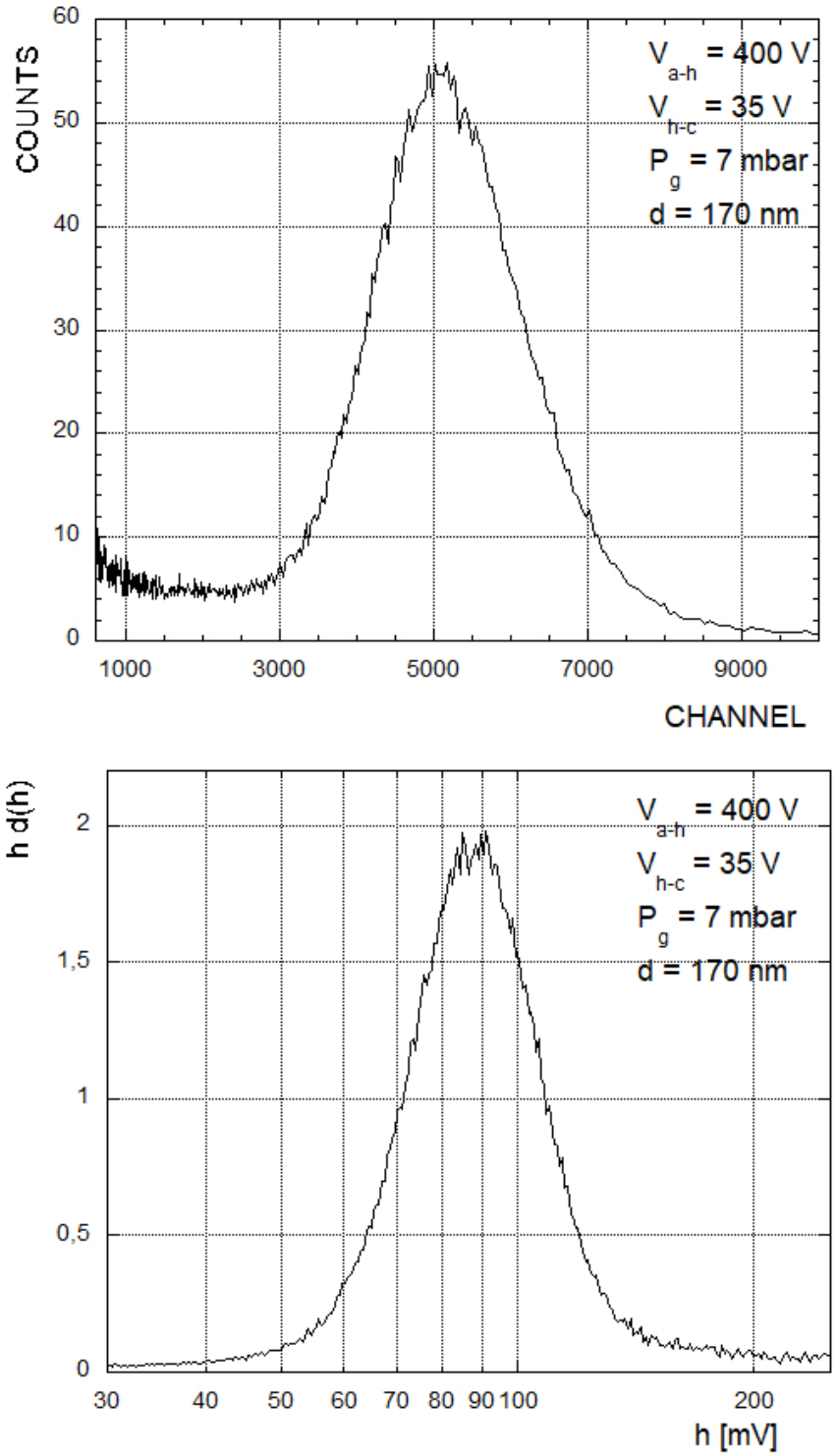

Figure 5.8: (Top) Example of TEPC alpha spectrum obtained with a 7 mbar gas pressures, corresponding to a 170 nm site size and the corresponding microdosimetric alpha spectrum $h\,d(h) - h$ in mV (bottom). See text for details.

5.3.2 Lineal Energy Calibration

The raw pulse height spectra, $h\,[\mathrm{mV}]$, of common TEPCs are usually calibrated in terms of lineal energy, $y\,[\mathrm{keV}\mu\mathrm{m}^{-1}]$, by exploiting an external radiation field (edge technique).
In particular, in the microdosimetric spectrum one has to identify some specific markers. For example, in a neutron field it is possible to recognize the position of the proton edge, which corresponds to the maximum amount of energy imparted by protons in the sensitive volume. In a photon field, the maximum lineal energy due to electrons that stop exactly at the border of the sensitive volume (exact stoppers), named electron edge, can be identified.
In order to calibrate the counter response, when the simulated diameter is of the order of 1 μm the literature [5] advices mono-energetic x-rays, which should have a sufficiently low energy so that the range of the secondary electrons is appreciably less than the effective diameter of the cavity. Alternatively, the exploitation of an alpha source is also possible.

This calibration procedure, though, is inadequate for our purpose as the maximum range (about 400 nm) of δ electrons set in motion by the ^{244}Cm alpha particles is greater than the counter cavity thickness. Because of that, the energy absorbed in the counters sensitive volume is less than the energy released. Since we are investigating site sizes down to a $10^1 - 10^2$ nanometer scale, such contributions have to be taken into account.
The theory of track structure distinguishes two different regions: core and penumbra [8] [42]. The core is a narrow central zone, with a radius in tissue far below $1\,\mu$m, where energy deposition events mainly occur in processes of excitation and electron plasma oscillation. The penumbra is a peripheral zone enveloping the core, where energy deposition is mainly due to ionization events induced by secondary energetic electrons. The extension of the penumbra depends in a complex manner on the maximum transferable energy to electrons, which in turns depends on the speed of the primary particle.

The absorbed energy between the helix and the cathode has been calculated by exploiting a numerical method, the Chatterjee model [43], that superimposes the counter sensitive volume geometry to the alpha particle track structure and calculates the percentage of the energy lost. The fraction $F(E)$ of the absorbed energy E_a to the released energy E_r results:

$$F(E) = \frac{E_a}{E_r} = \frac{1}{LET_\infty} \left[\int_0^{R_c} 2\pi r \, D_c(r) \, dr + \int_{R_c}^{R_p} 2\pi r \, A(r) \, dr \right] \tag{5.11}$$

where

- LET_∞ is the unrestricted Linear Energy Transfer;
- R_c and R_p are the core and penumbra radii, respectively, which are calculated via a semi-empirical formula;
- $D_c(r)$ and $D_p(r)$ are the local energy densities in the core and penumbra regions respectively, expressed as a function of the radial distance r from the centre of the track;
- $A(r)$ is the relative arc of a circumference centred on the particle track.

The radial extensions of both the core and the penumbra regions depend on the energy of the primary particle, whose value inside the sensitive volume has to be known in order to evaluate $F(E)$. The energy released in the counter E_r is calculated with an algorithm, which derives the energy lost by the alpha particle, before entering the sensitive volume and inside the sensitive volume itself, by exploiting the range-energy tables available in literature [44].

Unlike the absorbed energy, that depends only on the simulated site size, i.e. on the gas pressure, but is not affected by the applied voltages to the electrodes, the amplitude of the signal collected by the TEPC strongly depends on both the gas pressure and ΔV_{a-h}.
For this reason, a correlation between the energy of the alpha particle which is absorbed by the gas and the corresponding TEPC signal output was characterized as a function of the gas pressure and of the potential difference between the anode wire and the helix.
The energy calibration factor C_F, which depends on the simulated site size d_t

and on the voltages ΔV_{a-h} at the electrodes, is defined as:

$$CF(d_t, \Delta V_{a-h}) \left[\frac{keV}{mV}\right] = \frac{E_a}{V(d_t, \Delta V_{a-h})} \tag{5.12}$$

where V is the TEPC signal in mV.

The lineal energy, $y\,[\mathrm{keV}\mu\mathrm{m}^{-1}]$, is defined as the ratio of the energy imparted to the matter E_a and the mean chord length $\bar{l}$ of the sensitive volume (see Section 2.2.2). Since the active volume of MiMi2 is a right cylinder, the relation between the mean chord length and the diameter d_t of the simulated site is:

$$\bar{l} = \frac{2}{3}\, d_t \tag{5.13}$$

The lineal energy calibration factor is finally defined by:

$$LECF(d_t, \Delta V_{a-h}) \left[\frac{keV}{\mu m \cdot mV}\right] = \frac{3}{2}\, \frac{E_a}{d_t\, V(d_t, \Delta V_{a-h})} \tag{5.14}$$

5.3.3 Results

The values for the estimated released energy E_r, absorbed energy E_a and fraction F(E) together with the resulting LECF factor are listed in table 5.3 for every investigated gas pressure P_g, i.e. for every simulate site size d_t.

When using the lineal energy calibration factors, one should remember that,

P_g [mbar]	d_t [nm]	E_r [keV]	F(E)	E_a [keV]	V [mV]	LECF[$\frac{keV}{mV \cdot \mu m}$]
10	240	22.2	0.89	19.75	21.5	5.7
7.13	170	15.8	0.87	13.69	90.0	1.3
2.08	50	4.8	0.76	3.67	3.9	28.2
1.47	35	3.4	0.73	2.49	1.0	106.7

Table 5.3: Estimated released energy E_r, absorbed energy E_a and fraction F(E) together with the resulting LECF factor for every investigated gas pressure P_g, i.e. for every simulate site size d_t.

as its contributions depend both on the simulated site size d_t, i.e. on the gas pressure P_g, and on the ΔV_{a-h}, those are characteristic of the precise detector operating condition.

By exploiting the evaluated lineal energy calibration factor LECF, the microdosimetric spectra have been calibrated in $y\,[\mathrm{keV}\mu\mathrm{m}^{-1}]$.
Two examples of the resulting $yd(y) - y$ spectra, for the 170 and 50 nm simulated site size, are reported in Figure 5.9.
By analysing the spectra, one can see that their maxima attest at 120 ± 20 and 135 ± 30 keV/μm for the 170 and 50 nm simulated site size respectively, consistent with data known from literature [45]. Calculations with a Monte Carlo simulation code, in fact, indicate a 88 keV/μm energy loss for 5.9 MeV alpha particles in DME, which after the correction for the mean chord length of the crossing particles results coherent with the experimental results.

The two spectra have some clear differences, though. In particular, the 50 nm microdosimetric spectrum reveals both a broadening and the presence of a "bump" in the high lineal energy side of its $yd(y)$ distribution with respect to the 170 nm one.
The general broadening of the spectrum is due to the fact that in smaller simulated sites, i.e. in lower gas pressures, both the stochastic of the interaction and that of the gas avalanche formation are more relevant. The deformation of the spectrum caused by the bump could be due to the fact that alpha particles are not precisely mono-energetic. In particular, less energetic or scattered alpha particles completely stopping inside the sensitve volume could give rise to such higher y signals.

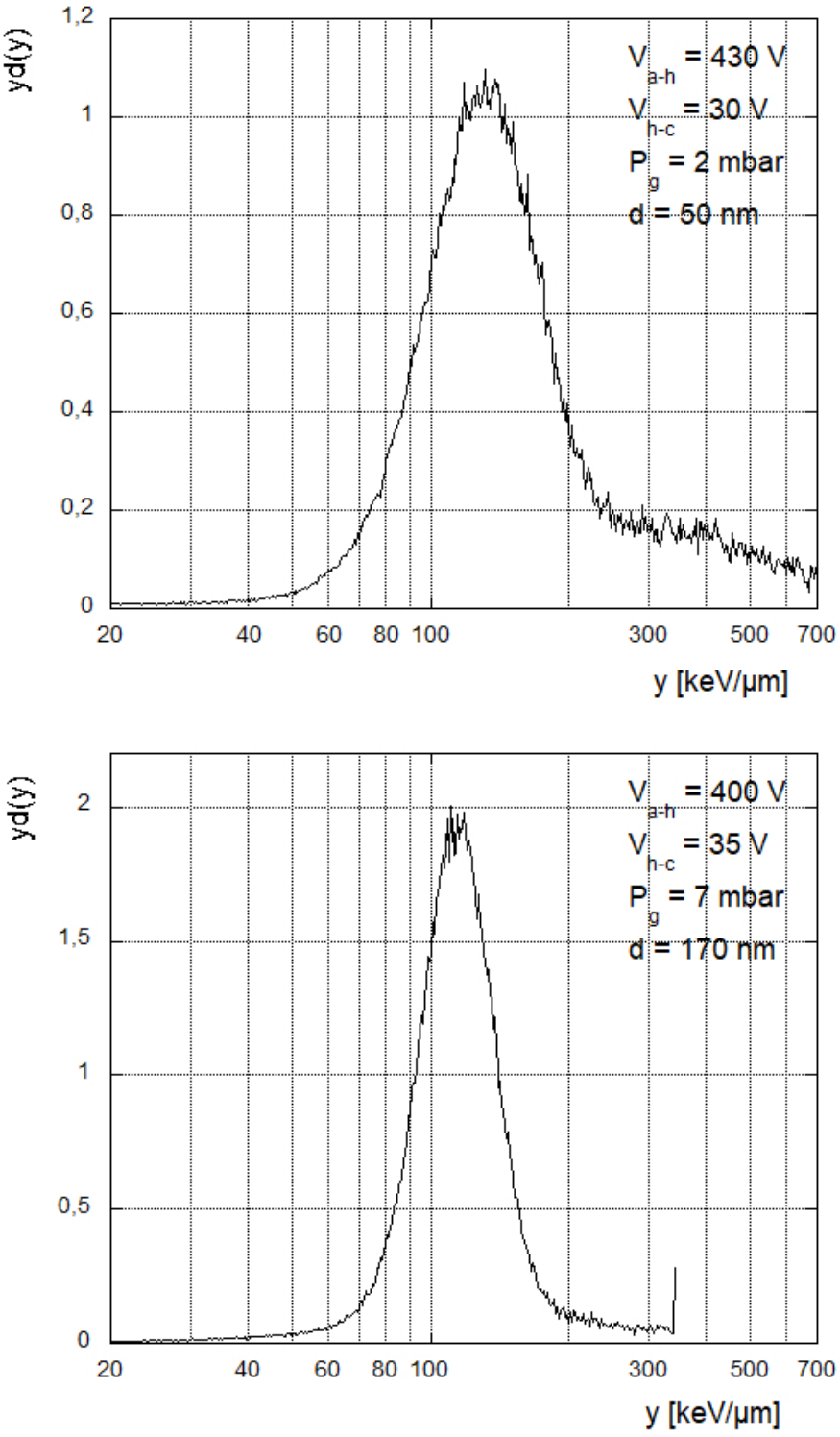

Figure 5.9: MiMi2 microdosimetric $yd(y) - y$ spectra obtained for a ^{244}Cm alpha source, with a 2 mbar (top) and a 7 mbar (bottom) gas pressures, corresponding to a 50 nm and a 170 nm site size. See text for details.

Chapter 6

Conclusions and future perspectives

A new avalanche-confinement Tissue Equivalent Proportional Counter named MiMi2, for calibration of microdosimetry at nanometer level on track-nanodosimetry, has been designed, constructed and installed in the Startrack apparatus at LNL.

The operation of the detector has been characterized by measurements with a ^{244}Cm alpha-particle source.
By varying the bias tension difference between the helix and cathode, it is possible to confine the avalanche region inside the helix so that the external volume included between the helix and the cathode electrodes is a pure drift region, meaning that the signal is independent on the position of the particle track. A good avalanche confinement results in a good energy resolution of the detector.
Depending on the gas pressure, optimal potential difference windows, namely the electron transmission windows, between helix and cathode have been determined.
Measurements have been successfully performed down to a simulated site size of 35 nm. In order to further decrease the site size, improvements in the performances of the preamplifier are necessary, in particular to increase the signal to noise ratio. Parallely, the possibility of biasing the anode electrode has to be investigated in order to achieve higher electric fields inside the avalanche region, meaning a higher gas gain.

The detector is now ready for characterization in accelerated ion beams. Simultaneous measurements with the StarTrack counter and MiMi2 will be performed for detailed investigation of unfolding procedures. The fluctuations of the signal detected by the TEPC result from the convolution of the stochastics of physical interaction processes with the stochastics of electronic avalanche formation. Pairwise measurements will allow to study the possibility to extract, from TEPC spectra, physical quantities that are significant for characterizing the particle track structure at nanonmeter level, much more relevant in the frame of biological damage.

Recent track structure investigations [25] highlighted a direct proportionality between the nanodosimetric cumulative distributions and the biological inactivation cross-sections.

In a similar way, cumulative spectral components of "nano-microdosimetry", such as the fraction of frequency or dose lineal energy distributions greater than a specific threshold level, could have a correlation with the biological outcome simpler than that produced by a weighting function.

If the comparison between micro- and nano-dosimetric spectra revealed an unfolding procedure able to separate the cumulative distribution informations from the stochastics of the avalanche formation, the exploitation of TEPCs in evaluating the therapeutic hadron beams quality could become way more accurate.

Bibliography

[1] D.T. Goodhead, *Initial events in the cellular effects of ionizing radiations: clustered damage in DNA*. International Journal of Radiation Biology, 65: 7-17 (1994).

[2] M. Durante, JS Loeffler, *Charged particles in radiation oncology*. Nature Reviews Clinical Oncology 7: 37-43 (2010).

[3] International Commission on Radiation Units and Measurement (ICRU), *Clinical Proton Dosimetry. Part I: beam production, beam delivery and measurement of absorbed dose*. Report 59, Bethesda (1998).

[4] International Atomic Energy Association (IAEA), *Relative biological effectiveness in ion beam therapy*. Technical Report Series (TSR) 461, Vienna, IAEA (2008).

[5] International Commission on Radiation Units and Measurement (ICRU), *Microdosimetry*. Report 36 (1983).

[6] H.H. Rossi, M. Zaider, *Microdosimetry and its applications*. Springer, New York (1996).

[7] B. Grosswendt, *Recent advances of nanodosimetry*. Radiation Protection Dosimetry 110: 789-799 (2004).

[8] International Commission on Radiation Units and Measurement (ICRU), *Linear Energy Transfer*, Report 16 (1970).

[9] H.H. Rossi, *Specification of radiation quality*. Radiation Research, 10(5): 522-531 (1959).

[10] A. Cauchy, *Memoire sur la rectification des courbes et la quadrature des sourfaces courbes*. Oevres Completes, Paris (1908).

[11] A. Wambersie, P. Pihet, H.G. Menzel, *The role of microdosimetry in radiotherapy*. Radiation Protection Dosimetry 31 (1-4): 421-432 (1990).

[12] P. Pihet et al., *Biological weighting function for RBE specification of neutron therapy beams. Intercomparison of 9 European Centres*. Radiation Protection Dosimetry 31: 437-442 (1990).

[13] T. Loncol et al., *Radiobiological effectiveness of radiation beams with broad LET spectra: microdosimetric analysis using biological weighting functions*. Radiation Protection Dosimetry 52 (1-4): 347-352 (1994).

[14] P. Kliauga, *Measurement of single event energy deposition spectra at 5nm to 250 nm simulated site sizes*. Radiation Protection Dosimetry 31 (1-4): 119-123 (1990).

[15] L. De Nardo et al., *Mini TEPCs for radiation therapy*. Radiation Protection Dosimetry 108 (4): 345-352 (2004a).

[16] A. Wambersie et al., *The RBE issues in ion-beam therapy: conclusions of a joint IAEA/ICRU working group regarding quantities and units*. Radiation Protection Dosimetry 122: 463-470 (2006).

[17] G. Garty et al., A nanodosimetric model of radiation-induced clustered DNA damage yields, Phys. Med. Biol. 55: 761-781 (2010).

[18] B. Grosswendt, *Nanodosimetry, from radiation physics to radiation biology*. Radiation Protection Dosimetry 115 (1-4): 1-9 (2005).

[19] H. Rabus, H. Nettelbeck, *Nanodosimetry: Bringing the gap to radiation biophysics*. Radiation Measurements 46: 1522-1528 (2011).

[20] A. Bantsar, *Ionization cluster size distributions created by low energy electrons and alpha particles in nanometric track segments in gases*. PhD Thesis (2011).

[21] H. Terato, H. Ide, *Clustered DNA damage induced by heavy ion particles*. Biological Sciences in Space 18 (4): 206-215 (2004).

[22] L. De Nardo, P. Colautti, V. Conte, W. Baek, B. Grosswendt, G. Tornielli,, *Ionization-cluster distributions of particles in nanometric volumes of propane: measurement and calculation*. Radiation and Environmental Biophysics 41 (4): 235-256 (2002).

[23] B. Grosswendt, L. De Nardo, P. Colautti, S. Pszona, V. Conte, G. Tornielli, *Experimental equivalent cluster-size distributions in nanometric volumes of liquid water*. Radiation Protection Dosimetry 110: 851-857 (2004).

[24] V. Conte, P. Colautti, B. Grosswendt, D. Moro, L. De Nardo, *Track structure of light ions: experiments and simulations*. New Journal of Physics 14 - 093010 (2012).

[25] V. Conte, A. Selva, P. Colautti, G. Hilgers, H. Rabus, A. Bantsar, M. Pietrzak, S. Pszona, *Nanodosimetry: towards a new concept of radiation quality*. Radiation Protection Dosimetry pp.1-7 (2017)

[26] L. De Nardo, A. Alkaa, C. Khamphan, V. Conte, P. Colautti, P. Sgur et al., *A detector for track-nanodosimetry*. Nuclear Instruments and Methods in Physics Research A 484: 312-326 (2002)

[27] B. Hogeweg, *Gas Gain Characteristics of a Tissue-Equivalent Proportional Counter, and their Implications for Measurements of Event Size Distributions in Small Volumes*. In Proc. Fourth Symp. on Microdosimetry, Volume 5122: 843-854 (1973).

[28] A.J. Waker, *Principles of experimental microdosimetry*. Radiation Protection Dosimetry 61(4): 297-308 (1995).

[29] L.J. Goodman, *Density and Composition Uniformity of A-150 tissue-equivalent plastic*. Physics in Medicine and Biology 23 (4): 753-758 (1978).

[30] U. Fano, *Note on the Bragg-Gray cavity principle for measuring energy dissipation*. Radiation Research 1(3):237-240 (1954).

[31] G. Knoll, *Radiation Detection and Measurements*. John Wiley and Sons (2010).

[32] A.N. Kontaratos, *On the functional dependence of Townsends first coefficient*. Applied Scientific Research, Section B, 12:27-32 (1965).

[33] D. Moro, *Development of tissue equivalent proportional counter for BNCT microdosimetry*. PhD Thesis, Universit degli studi di Ferrara, Italy (2006).

[34] P. Kliauga, A.J. Waker, J. Barthe, *Design of tissue-equivalent proportional counters*. Radiation Protection Dosimetry 61(4): 309-322 (1995).

[35] International Commission on Radiation Units and Measurement (ICRU), *Average energy required to produce an ion pair*. Report 31 (1979).

[36] V. Cesari, P. Colautti, G. Magrin, L. De Nardo, W. Y. Baek, B. Grosswendt, A. Alkaa, C. Khamphan, P. Sgur, G. Tornielli, *Nanodosimetric measurements with an avalanche confinement TEPC*. Radiation Protection Dosimetry 99(1-4): 337-342 (2002).

[37] D. Bortot, *A Novel Avalanche-Confinement TEPC for Microdosimetry at Nanometric Level*. PhD Thesis, Politecnico di Milano, Italy (2015).

[38] D. Bortot, D. Mazzucconi, M. Bonfant, S. Agosteo, A. Pola, S. Pasquato, A. Fazzi, P. Colautti and V. Conte, *A novel TEPC for microdosimetry at nanometric level: response against different neutron fields*. Radiation Protection Dosimetry 29:1-5 (2017).

[39] A. Alkaa, M.C. Bordage, V. Cesari, P. Colautti, V. Conte, L. De Nardo, P. Segur, G. Magrin, G. Tornielli, *A Code for Modelling Cylindrical TEPCs*. In: Radiation Quality Assessment Based on Physical Radiation Interaction at Nanometre Level. LNL-INFN (REP) 161/2000, pp.7192 (2000).

[40] V. Cesari, *Il TEPC con DME a bassa pressione nella microdosimetria per diametri simulati inferiori a 100 nanometri*. Masters Thesis, Universit degli Studi di Padova (1998).

[41] J.M. Meek *A theory of spark discharge*. Physical review 57, 722 (1940).

[42] A. Chatterjee, H. D. MacCabee, and C. A. Tobias, *Radial Cutoff LET and Radial Cutoff Dose Calculations for Heavy Charged Particles in Water*. Radiation Research 54:3, 479-494 (1973).

[43] A. ChatterjeeH, J. Schaefer, *Microdosimetric structure of heavy ion tracks in tissue*. Radiation and Environmental Biophysics 13:215 (1976).

[44] International Commission on Radiation Units and Measurement (ICRU), *Stopping powers and ranges for protons and alpha particles*. Report 49 (1994).

[45] J.F. Ziegler, M.D. Ziegler,J.P. Biersack, *SRIM - The stopping and range of ions in matter*. Nuclear Instruments and Methods in Physics Research, Section B, Volume 268, Issue 11-12, p. 1818-1823. (2010)